The Aerodynamics and Stability Analysis of a Vertical Tailless Aircraft with Rotary Horizontal Tail

Yifu Wang

A thesis
submitted in partial fulfillment of the
requirements for the degree of

Master of Science

University of Washington

2020

Committee:

Dana Dabiri

Mehran Mesbahi

Program Authorized to Offer Degree:
Aeronautics and Astronautics

University of Washington

Abstract

The Aerodynamics and Stability Analysis of a Vertical Tailless Aircraft with Rotary Horizontal Tail

Yifu Wang

Co-Chairs of the Supervisory Committee:
Professor Dana Dabiri
William E. Boeing Department of Aeronautics and Astronautics

Professor Mehran Mesbahi
William E. Boeing Department of Aeronautics and Astronautics

In this thesis, we explore the aerodynamic merits of replacing the vertical tail of the conventional aircraft with a rotary horizontal tail and identify the potential instability within the dynamics. The rigid body dynamics of a conventional aircraft and its vertical tailless version have been modeled for stability and control analysis. The nonlinear dynamics is linearized at trimmed flight conditions. For the conventional model, its spiral mode is unstable. For the vertical tailless model, its spiral mode and Dutch roll mode are unstable. A linear quadratic regulator is designed to resolve the instability. The aerodynamic data have been collected via software and wind tunnel to find the drag coefficient reduction. To ensure that we are comparing apples to apples, we have created three different flight scenarios where the force and moment coefficients of the conventional and vertical tailless aircraft are matched to the greatest extend. Results have shown that the total drag coefficient of the vertical tailless model is reduced by an average of 3.18% comparing to its conventional version during steady flight, 3.25% for steady level turn, and 10.4% for selected control surface deflection angles.

TABLE OF CONTENTS

LIST OF FIGURES

ACKNOWLEDGMENTS

I would like to express my sincere gratitude to Professor Dabiri and Professor Mesbahi for their patience, guidance, and support.

DEDICATION

To my parents and grandparents

Chapter 1

INTRODUCTION

The objective of this thesis is to explore the merits of replacing the vertical tail of the conventional aircraft with a rotary horizontal tail and identify the potential instability within the dynamics. The rigid body dynamics of the conventional aircraft and its vertical tailless version have been modeled for stability and control analysis. The aerodynamic data have been collected using both software and wind tunnel to find the drag coefficient reduction. Before proceeding with this, the history and incentives for vertical tailless configuration and some previous research results are presented in the following sections.

1.1 Incentives for Alternative Aircraft Design

The incentive for alternative aircraft design is to expand the design envelope of the conventional aircraft and eventually improve the aircraft performance. For instance, oblique wings and configurations with supersonic laminar flow are promising candidates for more efficient supersonic aircraft [2]. The photo of the oblique wing is shown in Fig. 1.1a. In the subsonic regime, the Boeing Blended-Wing-Body (BWB) airplane shows significant performance improvements over the conventional baseline with a 15% reduction in takeoff weight and a 27% reduction in fuel burn per seat-mile [3]. The photo of the Boeing X-48B wing body technology demonstrator is shown in Fig. 1.1b.

(a) AD-1 oblique wing. *Credits: NASA Photo*

(b) Boeing's X-48B Blended Wing Body technology demonstrator. *Credits: NASA Photo*

Figure 1.1: Examples of alternative aircraft design.

1.2 Tailless Aircraft

The problem of designing a tailless aircraft has been considered by aircraft designers for over a hundred years [4]. During this time, the techniques required to design a longitudinally stable tailless aircraft have been developed. The first longitudinal trim techniques is to use airfoil sections with large positive C_{m_0} and an example of this design approach is the Pathfinder as shown in Fig. 1.2a. The aircraft is stable in pitch with the elevons on the trailing edge of the wing as shown in Fig. 1.2b. The second trim technique is to use 3D effects through sweep and twist and an example of this design approach is the SWIFT foot-launched sailplane [5] as shown in Fig. 1.3a. The inboard flaps produces nose-up trim despite the large negative section moments. The third trim technique is to use active control and an example of this design approach is the Oblique Flying Wings as shown in Fig. 1.1a. While removing the tail results in drag reduction, it also introduces longitudinal and lateral-directional instability. Therefore, the tailless configuration has generally been considered as inferior to the conventional design.

(a) The Pathfinder. *Credits: NASA Photo*

(b) The elevons of the Pathfinder (yellow).

Figure 1.2: The Pathfinder and its control surfaces.

(a) Aeriane SWIFT Lite glider.

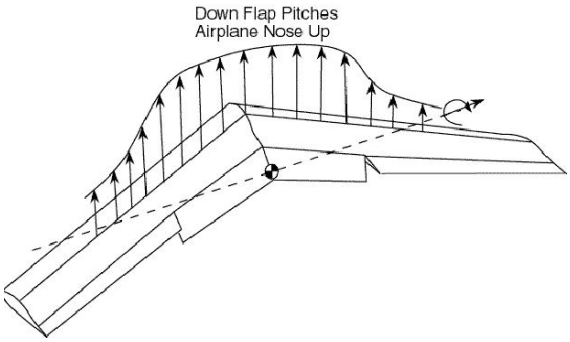

(b) The inboard flap produces nose-up trim despite the large negative section moments [5]

Figure 1.3: SWIFT foot-launched sailplane.

1.3 Vertical Tailless Aircraft

In order to accommodate with the dramatic budget cut in aerospace since the late 1980s, a national program aimed at advancing aerospace technology with limited resources is es-

tablished [6]. The goal of the program is to reduce air frame weight, improve aircraft lift to drag ratio, and improve aircraft agility while minimizing the total cost. One of the solutions to the problem is to eliminate the vertical tail. The vertical tailless configuration for fighters has been studied and several control challenges have been identified. Those challenges include yaw control power generation, multi-axis instabilities, and a large number highly coupled, nonlinear control effectors [6]. A controller was designed using dynamic inversion and μ-synthesis technique.

1.4 Vertical Tailless Aircraft with Rotary Horizontal Tail

Removing the entire tail greatly degrade the longitudinal and lateral stability. Only removing the vertical tail and having a horizontal tail that can rotate around its X body axis would be a more feasible solution because the rotating horizontal tail would generate force and moment that help stabilizing the aircraft in both longitudinal and lateral directions. The concept diagram of such aircraft is plotted as shown in Fig. 1.4.

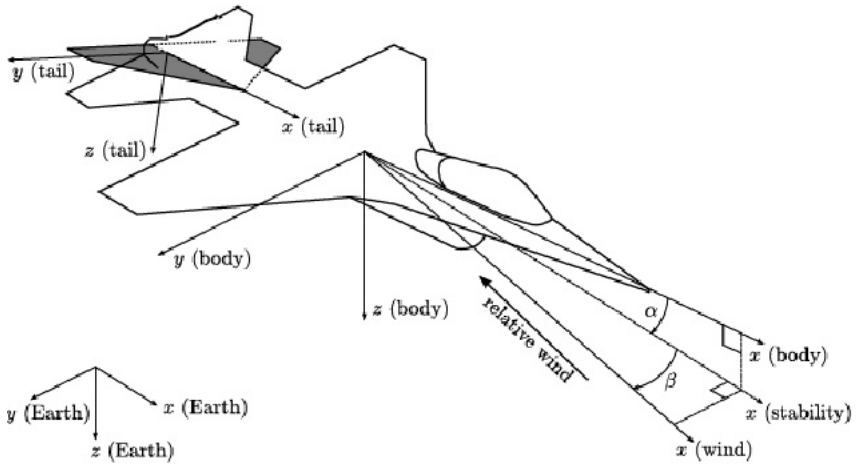

Figure 1.4: Vertical Tailless Aircraft with Rotary Horizontal Tail Concept [1].

1.5 Thesis Structure

The content of the thesis are presented according to the following outline. In Chapter 2, the nonlinear mathematical model is formulated for generic business jet in body-axes and stability-axes. Then, the trimmed condition for steady level flight is derived and used to find the linear state space model. In Chapter 3, a paper from 2013 [1] featuring flight dynamics and control of a vertical tailless aircraft is reviewed. The key equations of the mathematical model for vertical tailless configuration are carefully evaluated. In Chapter 4, an alternative method is presented to model the aerodynamics of the vertical tailless aircraft with better accuracy. Trimmed conditions are calculated and used to find the linear state space model. The unstable modes of the linearized system are identified using eigenvalue method and a feedback controller is synthesized to stabilize the aircraft. In Chapter 5, the data collected in wind tunnel are analyzed and the drag coefficient reduction between conventional and vertical tailless version are calculated for three comparable cases. Finally, in Chapter 6, the thesis is concluded with a brief summary of the results obtained and suggestions for future work.

Chapter 2

FLIGHT DYNAMICS OF A CONVENTIONAL AIRCRAFT

In this chapter, we will go over some key components for modeling the rigid body dynamics of the aircraft including the Euler angles, direction cosine matrices, body axes equations of motion. We will discuss the difference among body axes, wind axes and stability axes. Finally, we will construct the rigid body dynamics of a conventional aircraft and examine its longitudinal and lateral/directional stability.

2.1 Euler Angles

Euler angles represent the three dimensional orientation of an object with respect to a fixed coordinate system. The inertial frame is Earth-fixed and the body frame axes are aligned with the aircraft. The frame 1 and frame 2 are two intermediate frames. The inertial frame defines that the X-axis points North, the Y-axis points East, and the Z-axis points down as shown in Fig. 2.1. As a result, the inertial frame is also known as the North-East-Down (NED) frame.

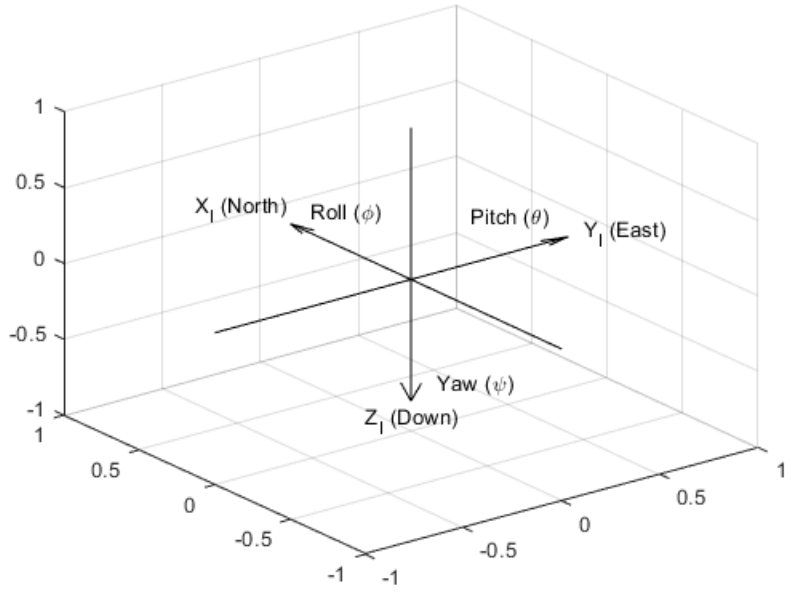

Figure 2.1: The Inertial Frame

As shown in Fig.2.1, yaw represents rotation about the inertial frame Z-axis by an angle of ψ. The yaw rotation produces a new coordinate frame where the Z-axis is aligned with the inertial frame and the X and Y axes are rotated by the yaw angle ψ. The orientation of the A1 frame after yaw rotation is shown in Fig. 2.2. The 1 frame is plotted in red and the inertial frame is plotted in grey.

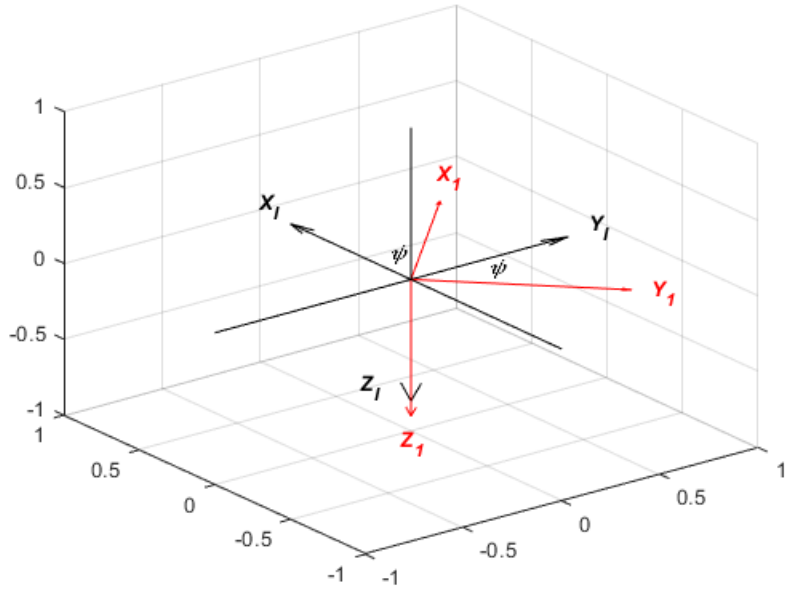

Figure 2.2: The Intermediate Frame 1

Pitch represents rotation about the 1 frame's Y-axis by an angle θ as shown in Fig. 2.3. The pitch rotation produces a new coordinate frame where the Y-axis is aligned with the inertial frame and the X and Z axes are rotated by the pitch angle θ. The orientation of the 2 frame after pitch rotation is shown in Fig. 2.3. The A frame is plotted in grey and the 2 frame is plotted in red.

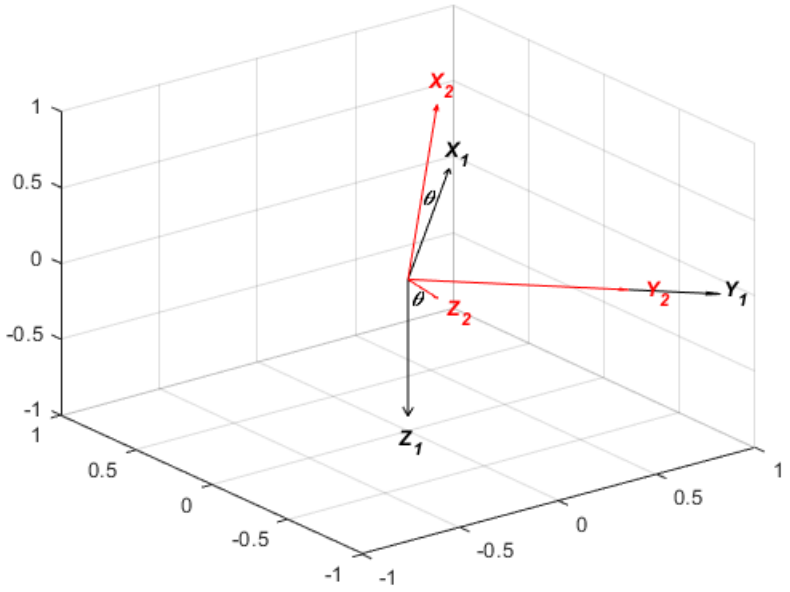

Figure 2.3: The Intermediate Frame 2

The body frame is aligned with the body of the aircraft. On an aircraft, the body frame X-axis points out the nose, the Y-axis points out the right side of the fuselage, and the Z-axis points out the bottom of the fuselage. The body frame is obtained by performing a rotation by the angle ϕ around the 2 frame's X-axis as shown in Fig. 2.4. The 2 frame is shown in gray and the body frame is shown in red.

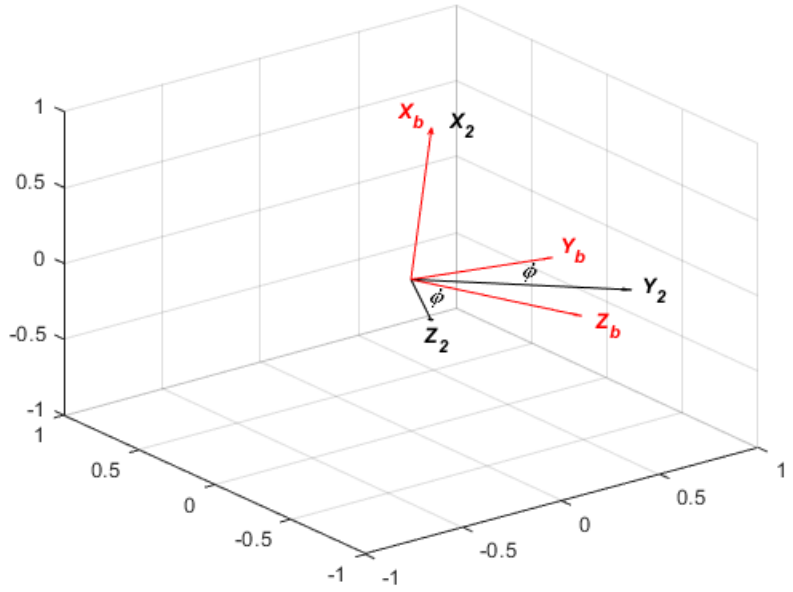

Figure 2.4: The Body Frame

2.2 Direction Cosine Transformation Matrices

Rotation of a vector from the Inertial Frame to the 1 Frame can be performed by multiplying the vector by the rotation matrix.

$$C_I^{v1}(\psi) = \begin{bmatrix} cos(\psi) & sin(\psi) & 0 \\ -sin(\psi) & cos(\psi) & 0 \\ 0 & 0 & 1 \end{bmatrix} \tag{2.1}$$

The rotation matrix for moving from the 1 frame to the 2 frame is given by

$$C_{v1}^{v2}(\theta) = \begin{bmatrix} cos(\theta) & 0 & -sin(\theta) \\ 0 & 1 & 0 \\ sin(\theta) & 0 & cos(\theta) \end{bmatrix} \tag{2.2}$$

The rotation matrix for moving from the inertial frame to the 2 frame consists simply of

the yaw matrix multiplied by the pitch matrix

$$C_I^{v2} = C_{v1}^{v2} C_I^{v1} \tag{2.3}$$

The rotation matrix for moving from the 2 frame to the body frame is given by

$$C_{v2}^{B}(\theta) = \begin{bmatrix} 1 & 0 & 0 \\ 0 & cos(\phi) & sin(\phi) \\ 0 & -sin(\phi) & cos(\phi) \end{bmatrix} \tag{2.4}$$

The complete rotation matrix for moving from the inertial frame to the body frame is given by

$$C_I^B = C_{v2}^B C_{v1}^{v2} C_I^{v1} \tag{2.5}$$

$$C_I^B = \begin{bmatrix} 1 & 0 & 0 \\ 0 & cos(\phi) & sin(\phi) \\ 0 & -sin(\phi) & cos(\phi) \end{bmatrix} \begin{bmatrix} cos(\theta) & 0 & -sin(\theta) \\ 0 & 1 & 0 \\ sin(\theta) & 0 & cos(\theta) \end{bmatrix} \begin{bmatrix} cos(\psi) & sin(\psi) & 0 \\ -sin(\psi) & cos(\psi) & 0 \\ 0 & 0 & 1 \end{bmatrix} \tag{2.6}$$

$$= \begin{bmatrix} c(\theta) & 0 & -s(\theta) \\ s(\phi)s(\theta) & c(\phi) & s(\phi)c(\theta) \\ c(\phi)s(\theta) & -s(\phi) & c(\phi)c(\theta) \end{bmatrix} \begin{bmatrix} cos(\psi) & sin(\psi) & 0 \\ -sin(\psi) & cos(\psi) & 0 \\ 0 & 0 & 1 \end{bmatrix} \tag{2.7}$$

$$= \begin{bmatrix} c(\theta)c(\psi) & c(\theta)s(\psi) & -s(\theta) \\ s(\phi)s(\theta)c(\psi) - c(\phi)s(\psi) & s(\phi)s(\theta)s(\psi) + c(\phi)c(\psi) & s(\phi)c(\theta) \\ c(\phi)s(\theta)c(\psi) + s(\phi)s(\psi) & c(\phi)s(\theta)s(\psi) - s(\phi)c(\psi) & c(\phi)c(\theta) \end{bmatrix} \tag{2.8}$$

The defined ranges for the rotation angles are

$$-\pi < \phi \leq \pi \tag{2.9}$$

$$-\frac{\pi}{2} \leq \theta \leq \frac{\pi}{2} \tag{2.10}$$

$$-\pi < \psi \leq \pi \tag{2.11}$$

2.3 Body-Axes Equations of Motion

In this section, the aerodynamics force and moment equations are combined with the vector equations of motion to obtain aircraft models for simulation purposes. The body-axes equations are preferable for general flight simulation.

The body-axes force equations are given as

$$\dot{U} = RV - QW - g_D \sin\theta + (X_A + X_T)/m \tag{2.12}$$

$$\dot{V} = -RU + PW + g_D \sin\phi \cos\theta + (Y_A + Y_T)/m \tag{2.13}$$

$$\dot{W} = QU - PV + g_D \cos\phi \cos\theta + (Z_A + Z_T)/m \tag{2.14}$$

The body-axes kinematic equations are given as

$$\dot{\phi} = P + Q \tan\theta \sin\phi + R \tan\theta \cos\phi \tag{2.15}$$

$$\dot{\theta} = Q \cos\phi + R \sin\phi \cos\theta \tag{2.16}$$

$$\dot{\psi} = Q \sin\phi / \cos\theta + R \cos\phi / \cos\theta \tag{2.17}$$

The body-axes moment equations are given as

$$\Gamma\dot{P} = J_{xz}(J_x - J_y + J_z)PQ - [J_z(J_z - J_y) + J_{xz}^2]QR + J_z l + J_{xz} n \tag{2.18}$$

$$J_y\dot{Q} = (J_z - J_x)PR - J_{xz}(P^2 - R^2) + m \tag{2.19}$$

$$\Gamma\dot{R} = [(J_x - J_y)J_x + J_{xz}^2]PQ - J_{xz}[J_x - J_y + J_z]QR + J_{xz} l + J_x n \tag{2.20}$$

$$\Gamma = J_x J_z - J_{xz}^2 \tag{2.21}$$

The body-axes navigation equations are given as

$$\begin{aligned} \dot{p}_N = {} & U \cos\theta \cos\psi + V(-\cos\phi \sin\psi + \sin\phi \sin\theta \cos\psi) \\ & + W(\sin\phi \sin\psi + \cos\phi \sin\theta \cos\psi) \end{aligned} \tag{2.22}$$

$$\begin{aligned} \dot{p}_E = {} & U \cos\theta \sin\psi + V(\cos\phi \cos\psi + \sin\phi \sin\theta \sin\psi) \\ & + W(-\sin\phi \cos\psi + \cos\phi \sin\theta \sin\psi) \end{aligned} \tag{2.23}$$

$$\dot{p}_D = U \sin\theta - V \sin\phi \cos\theta - W \cos\phi \cos\theta \tag{2.24}$$

2.4 Stability-axes and Wind-axes

The aerodynamic forces and moments on an aircraft are produced by the relative motion with respect to the air and depend on the orientation of the aircraft with respect to the airflow. The two orientation angles are the angle of attack (α) and sideslip angle (β). As illustrated in [7] page 76, the figure shows an aircraft with the relative wind on its right side. The stability axes is obtained by rotating the body axes around the body Y-axis by the angle α. α is positive when the relative wind is under the aircraft. The wind axes is obtained by rotating the stability axes around the stability Z-axis by the angle β. β is positive when the relative wind is on the right side of the airplane.

Using the rules for finding rotation matrices in the section 2.1, the rotation matrices from body axes to stability axes is expressed in terms of α and the rotation matrices from stability axes to wind axes is expressed in terms of β.

$$C_B^S = \begin{bmatrix} \cos\alpha & 0 & \sin\alpha \\ 0 & 1 & 0 \\ -\sin\alpha & 0 & \cos\alpha \end{bmatrix} \tag{2.25}$$

$$C_S^W = \begin{bmatrix} \cos\beta & \sin\beta & 0 \\ -\sin\beta & \cos\beta & 0 \\ 0 & 0 & 1 \end{bmatrix} \tag{2.26}$$

Thus, the complete rotation from body axes to wind axes is given as

$$C_B^W = C_B^S C_S^W = \begin{bmatrix} \cos\alpha\cos\beta & \sin\beta & \sin\alpha\cos\beta \\ -\cos\alpha\sin\beta & \cos\beta & -\sin\alpha\sin\beta \\ -\sin\alpha & 0 & \cos\alpha \end{bmatrix} \tag{2.27}$$

2.5 Stability-Axes Equations

For linearizing the equations of motion and studying the dynamic behavior, it is preferable to express the aircraft models in terms of stability/wind-axes variables. Under certain conditions, the stability/wind-axes equations decouple into two sets of equation, one describing the longitudinal motion and the other describing the lateral-directional motion.

The stability/wind-axes force equations are given as

$$m\dot{V}_T = F_T \cos(\alpha + \alpha_T)\cos\beta - D + mg_1 \tag{2.28}$$

$$m\dot{\beta}V_T = -F_T \cos(\alpha + \alpha_T)\sin\beta - C + mg_2 - mV_T R_s \tag{2.29}$$

$$m\dot{\alpha}V_T \cos\beta = -F_T \sin(\alpha + \alpha_T) - L + mg_3 + mV_T(Q\cos\beta - P_s \sin\beta) \tag{2.30}$$

The stability/wind-axes moment equations are given as

$$\begin{bmatrix} \dot{P}_s \\ \dot{Q} \\ \dot{R}_s \end{bmatrix} = -\dot{\alpha} \begin{bmatrix} -R_s \\ 0 \\ P_s \end{bmatrix} + \frac{1}{\Gamma} \begin{bmatrix} J'_Z & 0 & J'_{xz} \\ 0 & \Gamma/J'_y & 0 \\ J'_{xz} & 0 & J'_x \end{bmatrix} \left(\begin{bmatrix} l_S \\ m \\ n_S \end{bmatrix} - \tilde{\omega}^S_{B/I} J^S \omega^S_{B/I} \right) \tag{2.31}$$

2.6 Linear State Space Model

A summary of flat-earth equation of motion in body axes is presented in section 2.3. In this section, we express the longitudinal and lateral-directional equation in the stability axes that is more intuitive than the body axes equation.

A fourth-order model whose state, control, and disturbance vector are

$$\Delta x_L = \begin{bmatrix} \Delta V & \Delta\gamma & \Delta q & \Delta\alpha \end{bmatrix}^T \tag{2.32}$$

$$\Delta u_L = \begin{bmatrix} \Delta E & \Delta T & \Delta F & \Delta S \end{bmatrix}^T \tag{2.33}$$

$$\Delta w_L = \begin{bmatrix} \Delta V_w & \Delta\alpha_w \end{bmatrix}^T \tag{2.34}$$

captures all the major longitudinal dynamics for rigid body motion.

The generalized linear state space model is given as

$$\Delta\dot{x}_L = A_L \Delta x_L + B_L \Delta u_L + L_L \Delta w_L \tag{2.35}$$

where

$$A_L = \begin{bmatrix} -D_V & -g\cos\gamma_0 & -D_q & -D_\alpha \\ \frac{L_V}{V_0+L_{\dot\alpha}} & \frac{g\sin\gamma_0}{V_0} & \frac{L_q}{V_0+L_{\dot\alpha}} & \frac{L_\alpha}{V_0+L_{\dot\alpha}} \\ M_V - aL_V & 0 & M_q - a(L_q - V_0) & M_\alpha - aL_\alpha \\ \frac{-L_V}{V_0+L_{\dot\alpha}} & \frac{-g\sin\gamma_0}{V_0} & \frac{V_0-L_q}{V_0+L_{\dot\alpha}} & \frac{-L_\alpha}{V_0+L_{\dot\alpha}} \end{bmatrix}, a = \frac{M_{\dot\alpha}}{V_0 + L_{\dot\alpha}} \tag{2.36}$$

$$B_L = \begin{bmatrix} -D_{\delta E} & T_{\delta T} & -D_{\delta F} & -D_{\delta S} \\ \frac{L_{\delta E}}{V_0+L_{\dot\alpha}} & \frac{L_{\delta T}}{V_0+L_{\dot\alpha}} & \frac{L_{\delta F}}{V_0+L_{\dot\alpha}} & \frac{L_{\delta S}}{V_0+L_{\dot\alpha}} \\ M_{\delta E} - aL_{\delta E} & M_{\delta T} - aL_{\delta T} & M_{\delta F} - aL_{\delta F} & M_{\delta S} - aL_{\delta S} \\ -\frac{L_{\delta E}}{V_0+L_{\dot\alpha}} & -\frac{L_{\delta T}}{V_0+L_{\dot\alpha}} & -\frac{L_{\delta F}}{V_0+L_{\dot\alpha}} & -\frac{L_{\delta S}}{V_0+L_{\dot\alpha}} \end{bmatrix} \tag{2.37}$$

$$L_L = \begin{bmatrix} D_V & D_\alpha \\ -\frac{L_V}{V_0+L_{\dot\alpha}} & -\frac{L_{alpha}}{V_0+L_{\dot\alpha}} \\ -M_V + aL_V & M_\alpha - aL_\alpha \\ \frac{L_V}{V_0+L_{\dot\alpha}} & \frac{L_\alpha}{V_0+L_{\dot\alpha}} \end{bmatrix} \tag{2.38}$$

The geometric details of the conventional aircraft is documented in [8]. The nonlinear conventional aircraft model is linearized at a steady level flight condition with an altitude of 10000 ft (3048 m) and a Mach number of 0.3. At the trimmed condition, the elevator deflection angle is $-3.46°$, the engine throttle is 18.8%, the angle of attack is $3.92°$.

Using MATLAB, the longitudinal 4th-order stability axes equation of motion is calculated as

$$\begin{aligned} \frac{d}{dt}\begin{bmatrix} V \\ \gamma \\ q \\ \alpha \end{bmatrix} &= \begin{bmatrix} -0.0186 & -9.8067 & -0.0656 & -8.1342 \\ 0.0021 & 0.0000 & 0.0099 & 1.2255 \\ 0.0000 & 0 & -1.2336 & -7.4366 \\ -0.0021 & -0.0000 & 0.9901 & -1.2255 \end{bmatrix}\begin{bmatrix} V \\ \gamma \\ q \\ \alpha \end{bmatrix} \\ &+ \begin{bmatrix} 0.0151 & 4.6702 \\ 12.2597 & 0 \\ -8.4455 & 0 \\ -12.2597 & 0 \end{bmatrix}\begin{bmatrix} dE \\ dT \end{bmatrix} \end{aligned} \tag{2.39}$$

where **V** is airspeed, $\boldsymbol{\gamma}$ is flight path angle, **q** is pitch rate, $\boldsymbol{\alpha}$ is angle of attack, **dE** is elevator deflection angle, **dT** is engine throttle.

The matrix associates with the state vector is the state matrix and the matrix relates to the control vector is the control matrix. From the state matrix, the eigenvalues and the eigenvectors of the matrix can be calculated.

The eigenvalues/poles are given as

$$\lambda_{1,2} = -0.0073 \pm 0.1298j \tag{2.40}$$

$$\lambda_{3,4} = -1.2316 \pm 2.7119j \tag{2.41}$$

The first and second eigenvalue correspond to the short-period mode. The third and fourth eigenvalue correspond to the phugoid mode. The natural frequency, damping ratio, and the period of each mode is calculated from the eigenvalues. It is observed that both short-period mode and phugiod mode are underdamped and stable.

$$\omega_{ph} = 0.12997 rad/s \tag{2.42}$$

$$T_{ph} = 48.344 s \tag{2.43}$$

$$\zeta_{ph} = 0.055926 \tag{2.44}$$

$$\omega_{sp} = 2.9785 rad/s \tag{2.45}$$

$$T_{sp} = 2.1095 s \tag{2.46}$$

$$\zeta_{sp} = 0.4135 \tag{2.47}$$

A fourth-order model whose state, control, and disturbance vector are

$$\Delta x_{LD} = \begin{bmatrix} \Delta r & \Delta\beta & \Delta q & \Delta\phi \end{bmatrix}^T \tag{2.48}$$

$$\Delta u_{LD} = \begin{bmatrix} \Delta A & \Delta R & \Delta AS \end{bmatrix}^T \tag{2.49}$$

$$\Delta w_{LD} = \begin{bmatrix} \Delta\beta_w & \Delta p_w \end{bmatrix}^T \tag{2.50}$$

captures all the major lateral-directional dynamics for rigid body motion.

The generalized lateral-directional linear state space model is given as

$$\Delta \dot{x}_{LD} = A_{LD}\Delta x_{LD} + B_{LD}\Delta u_{LD} + L_{LD}\Delta w_{LD} \tag{2.51}$$

where

$$A_{LD} = \begin{bmatrix} N_r + \frac{(Y_r - V_0)N_{\dot{\beta}}}{V_0} & N_\beta + \frac{Y_\beta N_{\dot{\beta}}}{V_0} & N_p + \frac{Y_p N_{\dot{\beta}}}{V_0} & N_\phi \\ \frac{(Y_r - V_0)}{V_0} & \frac{Y_\beta}{V_0} & \frac{Y_p}{V_0} & \frac{g_0 \cos\gamma_0}{V_0} \\ L_r & L_\beta & L_p & L_\phi \\ -\sin\gamma_0 & 0 & 1 & 0 \end{bmatrix} \tag{2.52}$$

$$B_{LD} = \begin{bmatrix} N_{\delta A} + \frac{Y_{\delta A} N_{\dot{\beta}}}{V_0} & N_{\delta R} + \frac{Y_{\delta R} N_{\dot{\beta}}}{V_0} & N_{\delta AS} + \frac{Y_{\delta AS} N_{\dot{\beta}}}{V_0} \\ \frac{Y_{\delta A}}{V_0} & \frac{Y_{\delta R}}{V_0} & \frac{Y_{\delta AS}}{V_0} \\ L_{\delta A} & L_{\delta A} & L_{\delta AS} \\ 0 & 0 & 0 \end{bmatrix} \tag{2.53}$$

$$L_{LD} = \begin{bmatrix} -(N_\beta + \frac{Y_\beta N_{\dot{\beta}}}{V_0}) & -(N_p + \frac{Y_p N_{\dot{\beta}}}{V_0}) \\ -\frac{Y_\beta}{V_0} & -\frac{Y_\beta}{V_0} \\ -L_\beta & -L_p \\ 0 & 0 \end{bmatrix} \tag{2.54}$$

Using MATLAB, the lateral/directional linear state space model is calculated as

$$\begin{aligned} \frac{d}{dt}\begin{bmatrix} r \\ \beta \\ p \\ \phi \end{bmatrix} &= \begin{bmatrix} -0.1084 & 1.7848 & 0.0631 & 0 \\ -1.0000 & -0.1513 & 0 & 0.0993 \\ 0.2590 & -2.2370 & -1.1192 & 0 \\ 0.0000 & 0 & 1.0024 & 0 \end{bmatrix}\begin{bmatrix} r \\ \beta \\ p \\ \phi \end{bmatrix} \\ &+ \begin{bmatrix} 0.2189 & -1.0317 \\ -0.1481 & 3.2759 \\ 4.2963 & 0.2320 \\ 0 & 0 \end{bmatrix}\begin{bmatrix} dA \\ dR \end{bmatrix} \end{aligned} \tag{2.55}$$

where **r** is yaw rate, $\boldsymbol{\beta}$ is sideslip angle, **p** is roll rate, $\boldsymbol{\phi}$ is bank angle, **dA** is aileron deflection angle, **dR** is rudder deflection angle.

From the state matrix A, the eigenvalues are calculated as

$$\lambda_1 = 0.0103 \tag{2.56}$$

$$\lambda_{2,3} = -0.1145 \pm 1.3458j \tag{2.57}$$

$$\lambda_4 = -1.1603 \tag{2.58}$$

The first eigenvalue corresponds to the spiral mode. The second and third eigenvalues correspond to the Dutch roll mode.The fourth eigenvalue correspond to the roll mode. It is shown that the spiral mode is unstable. The Dutch roll and roll modes are stable.

The time constant, natural frequencies, periods, and damping ratios of these modes are calculated as

$$\tau_{spiral} = 96.6885s \tag{2.59}$$

$$\tau_{roll} = 0.83096s \tag{2.60}$$

$$\omega_{Dutchroll} = 1.3507rad/s \tag{2.61}$$

$$T_{Dutchroll} = 4.652s \tag{2.62}$$

$$\zeta_{Dutchroll} = 0.08474 \tag{2.63}$$

In this chapter, we presented the fundamental equations for modeling the nonlinear rigid body dynamics of aircraft. We also examined the longitudinal and lateral/directional stability of an conventional aircraft. In the next chapter, we will review a closely related reference paper and have a discussion on its method, process and results.

Chapter 3

REVIEW OF A PAPER ABOUT VERTICAL TAILLESS AIRCRAFT

In 2013, Bras et al. [1] publish their findings on the study of a vertical tailless aircraft with rotary horizontal tail. In this paper [1], different tail configurations are analyzed in terms of static and dynamic stability and compared with the conventional configuration. The aircraft mathematical model is developed and some of the equations are summarized in section 3.1. Feedback control systems including a sideslip suppression system, a heading control system and a speed and altitude hold system are implemented for difference tail configurations. The results show that the tailless aircraft is statically stable and lateral-directional unstable without a controller.

3.1 Key Equations

In this section, a summary of the key equations used in [1] for vertical tailless aircraft dynamics model is presented.

The transformation from body-axes to stability axes of the velocity vector in the body-axes is given as

$$V_{Stability} = \begin{bmatrix} \cos\alpha & 0 & \sin\alpha \\ 0 & 1 & 0 \\ -\sin\alpha & 0 & \cos\alpha \end{bmatrix} V_{Body} \tag{3.1}$$

The transformation from stability-axes to wind-axes of the velocity vector is given as

$$V_{Wind} = \begin{bmatrix} \cos\beta & \sin\beta & 0 \\ -\sin\beta & \cos\beta & 0 \\ 0 & 0 & 1 \end{bmatrix} V_{Stability} \tag{3.2}$$

The transformation from wind to body axes is expressed as

$$V_{Body} = \begin{bmatrix} V_T \cos\alpha \cos\beta \\ V_T \sin\beta \\ V_T \sin\alpha \cos\beta \end{bmatrix} \tag{3.3}$$

The transformation from body to wing-axes is given as

$$V_{Wing} = \begin{bmatrix} \cos i_w & 0 & -\sin i_w \\ 0 & 1 & 0 \\ \sin i_w & 0 & \cos i_w \end{bmatrix} V_{Body} \tag{3.4}$$

For conventional horizontal tail, the rotation from wind to body-axes is given as

$$V_{Tail} = \begin{bmatrix} V_{Th} \cos\alpha_h \cos\beta \\ V_{Th} \sin\beta \\ V_{Th} \sin\alpha_h \cos\beta \end{bmatrix} \tag{3.5}$$

The transformation from the horizontal tail axes to rotated tail axes is

$$V_{rottail} = \begin{bmatrix} 1 & 0 & 0 \\ 0 & \cos\delta_h & \sin\delta_h \\ 0 & -\sin\delta_h & \cos\delta_h \end{bmatrix} V_{horiztail} \tag{3.6}$$

Consider small angle of attack and sideslip angle, the angle of attack for rotated tail is given as

$$\alpha_h = \frac{i_h - \beta \sin\delta_h + (\alpha - \epsilon)\cos\delta_h}{1 + i_h \beta \sin\delta_h - i_h(\alpha - \epsilon\cos\delta_h)} \tag{3.7}$$

where i_h is the tail incidence angle and ϵ is the tail downwash angle.

The force and moment transformation from stability axes to body axes for wings are given as

$$\begin{bmatrix} X \\ Y \\ Z \end{bmatrix} = \begin{bmatrix} \cos\alpha_w & 0 & -\sin\alpha_w \\ 0 & 1 & 0 \\ \sin\alpha_w & 0 & \cos\alpha_w \end{bmatrix} \begin{bmatrix} -D_w \\ 0 \\ -L_w \end{bmatrix} \tag{3.8}$$

$$\begin{bmatrix} L \\ M \\ N \end{bmatrix} = \begin{bmatrix} x_w \\ 0 \\ z_w \end{bmatrix} \times \begin{bmatrix} X \\ Y \\ Z \end{bmatrix} \tag{3.9}$$

The force and moment transformation from stability axes to body axes for tail are given as

$$\begin{bmatrix} X \\ Y \\ Z \end{bmatrix} = \begin{bmatrix} \cos\alpha_h & 0 & -\sin\alpha_h \\ -\sin\delta_h \sin\alpha_h & \cos\delta_h & -\cos\alpha_h \sin\delta_h \\ \cos\delta_h \sin\alpha_h & \sin\delta_h & \cos\delta_h \cos\alpha_h \end{bmatrix} \begin{bmatrix} -D_h \\ 0 \\ -L_h \end{bmatrix} \tag{3.10}$$

$$\begin{bmatrix} L \\ M \\ N \end{bmatrix} = \begin{bmatrix} -x_h \\ y_h \\ z_h \end{bmatrix} \times \begin{bmatrix} X \\ Y \\ Z \end{bmatrix} \tag{3.11}$$

3.2 Discussion

Eq. 3.1 and Eq. 3.2 use the same direction cosine matrices as we discussed in section 2.4 for transformation between wind axes and body axes. Bras et al. also use Eq. 3.4 to account for the wing incidence. The direction cosine matrix in Eq. 3.6 is analogous to Eq. 2.4 in section 2.2. As for Eq. 3.8, the direction cosine matrix is not proper because of the following reason. From the notation, it's clear that D_w and L_w represent the wing aerodynamic forces measured in wind axes. Whereas X, Y, and Z stand for aerodynamic forces measured in body axes. In order to perform transformation from wind axes to body axes, the inverse matrix of Eq. 2.27 is used. Similarly for Eq. 3.10, to transform the tail aerodynamic forces $-D_h$ and $-L_h$ in the wind axes to tail aerodynamic forces on the body axes. The direction cosine matrix is equal to Eq. 3.6 multiply with the inverse of Eq. 2.27. From the equations listed above it is evident that their aerodynamic force coefficients are calculated using equations that are based on small angle approximation and thin airfoil theory. The aerodynamic coefficients are estimated separately for the major components of the aircraft and summed together to represent for the entire aircraft. The effect of the horizontal tail rotation is incorporated through Eq. 3.7. Thus, the accuracy of the aerodynamic model

highly depends on the accuracy of Eq. 3.7. Since no derivation and reference are found for Eq. 3.7, the α_h vs. δ_h diagrams are plotted to verify if the relationship between tail angle of attack and tail rotation angle is properly described by the equation. Assuming that the tail incidence angle i_h, the sideslip angle β, and tail downwash angle ϵ are zero, the change of tail angle of attack with respect to tail rotation angle is plotted as shown in Fig. 3.1. It is shown that when the tail rotation angle is zero, the tail angle of attack is equal to the aircraft angle of attack. The tail angle of attack approaches zero as the tail rotation angle approaches 90°. All of these observations agree with the trend that tail lift coefficient decreases monotonically with tail rotation angles. However, their method only consider the aerodynamic forces generated by the wing and tail and neglect the contribution from other part of the aircraft. As a result, an alternative approach is presented in the next chapter to model the aerodynamics of the vertical tailless aircraft.

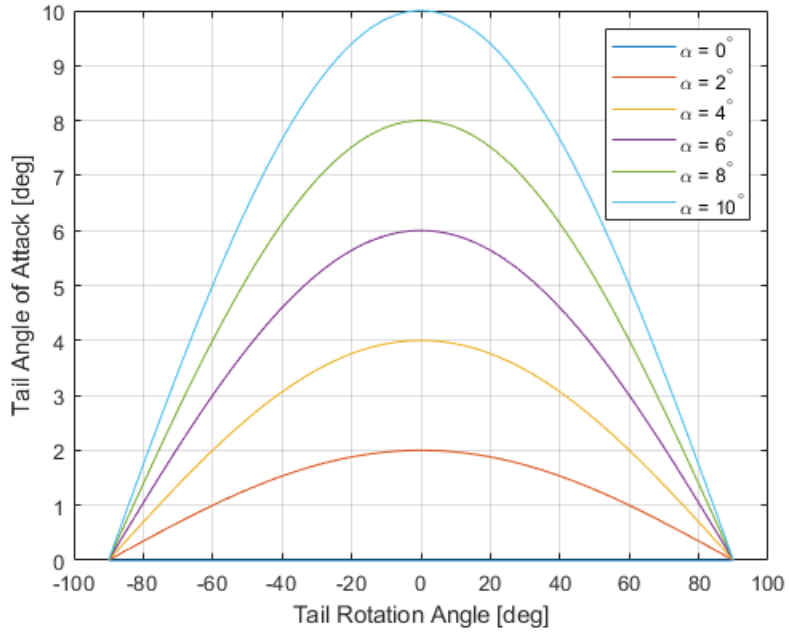

Figure 3.1: Tail angle of attack vs. Tail rotation angle

Chapter 4

FLIGHT DYNAMICS AND CONTROL OF A VERTICAL TAILLESS AIRCRAFT

In this chapter, first we obtain the aerodynamic model of the vertical tailless version of generic business jet. Secondly, we analyze the static stability of the aircraft using the aerodynamic data generated. Thirdly, we linearize the model at trim condition and decouple the system with respect to longitudinal and lateral/direction motion. Lastly, we identify the instability of the open-loop system and implement controllers to stabilize it.

4.1 Aerodynamic Model of the Vertical Tailless Aircraft

Before accessing the flight dynamics of the vertical tailless aircraft, we need to update the aerodynamic model due to removing the vertical tail. For convention aircraft, the aerodynamic force/moment coefficients are estimated in terms of aerodynamic derivatives. For instance, the sideforce coefficient is estimated as Eq. 4.1

$$C_Y = C_Y(\alpha,\beta,M) + \Delta C_{Y_{\delta_r}}(\alpha,\beta,M,\delta_r) + \Delta C_{Y_{\delta_a}}(\alpha,\beta,M,\delta_a) + \frac{b}{2V_T}[C_{Y_p}(\alpha,M)P + C_{Y_r}(\alpha,M)R] \quad (4.1)$$

where

$$C_Y(\alpha,\beta,M) \approx C_{Y_\beta}(\alpha,M) \times \beta \quad (4.2)$$

$$\Delta C_{Y_{\delta_r}}(\alpha,\beta,M,\delta_r) \approx C_{Y_{\delta_r}}(\alpha,\beta,M) \times \delta_r \quad (4.3)$$

$$\Delta C_{Y_{\delta_a}}(\alpha,\beta,M,\delta_a) \approx C_{Y_{\delta_a}}(\alpha,\beta,M) \times \delta_a \quad (4.4)$$

Since the vertical tail is removed and a rotary horizontal tail is attached at the end of the fuselage, Eq. 4.1 is no longer applicable and we need to derive new equations for estimating

coefficients. The alternative aerodynamics modelling method is adapted from [9]. By removing the terms related to rudder and adding terms related to rotary tail, the aerodynamic model is defined as follows

$$C_L = C_{L,base}(\alpha,\beta) + \Delta C_{L,q}(\alpha,\hat{q}) + \Delta C_{L,ele}(\alpha,\beta,\delta_E) + \Delta C_{L,ail}(\alpha,\beta,\delta_A) + \Delta C_{L,tail}(\alpha,\beta,\delta_{tail}) \quad (4.5)$$

$$C_D = C_{D,base}(\alpha,\beta) + \Delta C_{D,q}(\alpha,\hat{q}) + \Delta C_{D,ele}(\alpha,\beta,\delta_E) + \Delta C_{D,ail}(\alpha,\beta,\delta_A) + \Delta C_{D,tail}(\alpha,\beta,\delta_{tail}) \quad (4.6)$$

$$C_Y = C_{Y,base}(\alpha,\beta) + \Delta C_{Y,p}(\alpha,\hat{p}) + \Delta C_{Y,r}(\alpha,\hat{r}) + \Delta C_{Y,ail}(\alpha,\beta,\delta_A) + \Delta C_{Y,tail}(\alpha,\beta,\delta_{tail}) \quad (4.7)$$

$$C_l = C_{l,base}(\alpha,\beta) + \Delta C_{l,p}(\alpha,\hat{p}) + \Delta C_{l,r}(\alpha,\hat{r}) + \Delta C_{l,ail}(\alpha,\beta,\delta_A) + \Delta C_{l,tail}(\alpha,\beta,\delta_{tail}) \quad (4.8)$$

$$C_m = C_{m,base}(\alpha,\beta) + \Delta C_{m,q}(\alpha,\hat{q}) + \Delta C_{m,ele}(\alpha,\beta,\delta_E) + \Delta C_{m,ail}(\alpha,\beta,\delta_A) + \Delta C_{m,tail}(\alpha,\beta,\delta_{tail}) \quad (4.9)$$

$$C_n = C_{n,base}(\alpha,\beta) + \Delta C_{n,p}(\alpha,\hat{p}) + \Delta C_{n,r}(\alpha,\hat{r}) + \Delta C_{n,ail}(\alpha,\beta,\delta_A) + \Delta C_{n,tail}(\alpha,\beta,\delta_{tail}) \quad (4.10)$$

where $C_{(),base}(\alpha,\beta)$ are the baseline coefficients found at different angle of attack and sideslip angle, $C_{(),q}(\alpha,\hat{p}/\hat{q}/\hat{r})$ are coefficients found at different angle of attack and roll/pitch/yaw rate, $\Delta C_{(),q}(\alpha,\hat{p}/\hat{q}/\hat{r}) = C_{(),q}(\alpha,\hat{p}/\hat{q})/\hat{r} - C_{(),base}(\alpha,\beta)$. The coefficients are found using $VLAERO{+}^{TM}$ which is a computational fluid dynamics software based on the vortex lattice

method (VLM). The $VLAERO+^{TM}$ model of the generic business jet and its vertical tailless version are plotted as shown in Fig. 4.1.

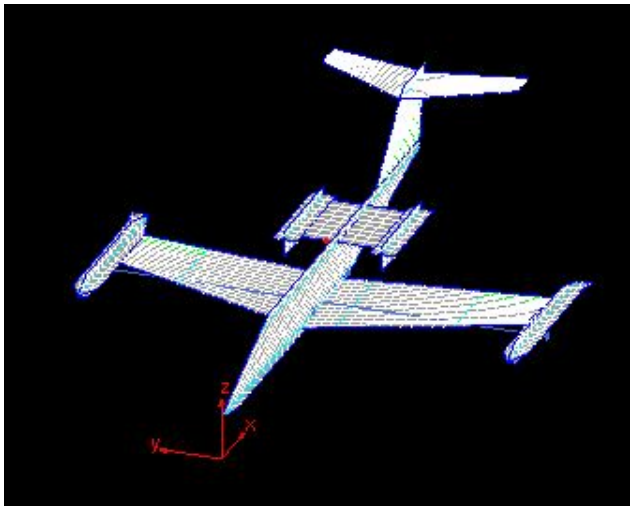

(a) Conventional business jet

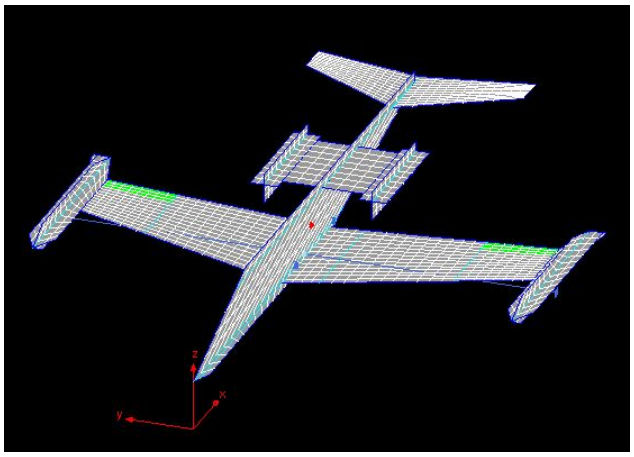

(b) Vertical tailless version

Figure 4.1: Generic business jet and its vertical tailless version modeled in VLAERO+

4.2 Static Stability

Given the aerodynamic data we collected in the previous section, we plot the aerodynamic force and moment coefficients over angle of attack and side-slip angle. By accessing the slope of the moment coefficient curves, we found aerodynamic derivatives that indicate static stability in roll, pitch, and yaw direction. The aerodynamic force and moment coefficients of the conventional and tailless aircraft are plotted as shown in Fig. 4.2 - Fig. 4.7. The control surface deflection angles in those diagrams are zero unless otherwise specified. These diagrams provide some insight into how would the force and moment coefficients be affected by the tail rotation angle. From Fig. 4.5 - Fig. 4.7, it is observed that the static stability of the aircraft is also subjected to tail rotation. In order to obtain a better insight into the stability of the vertical tailless aircraft, we access the dynamic stability in the next section.

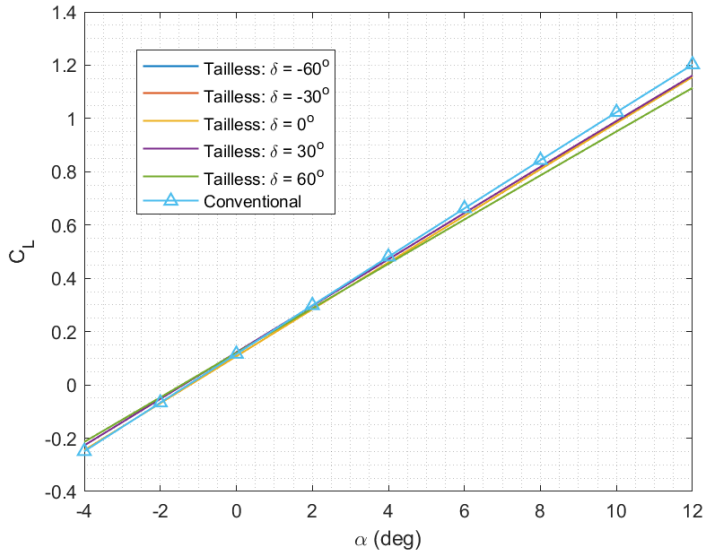

Figure 4.2: Lift coefficient vs. Angle of attack

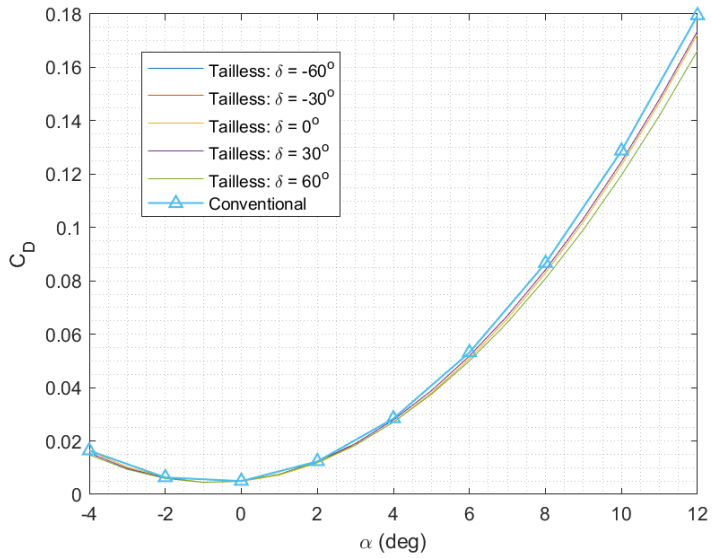

Figure 4.3: Drag coefficient vs. Angle of attack

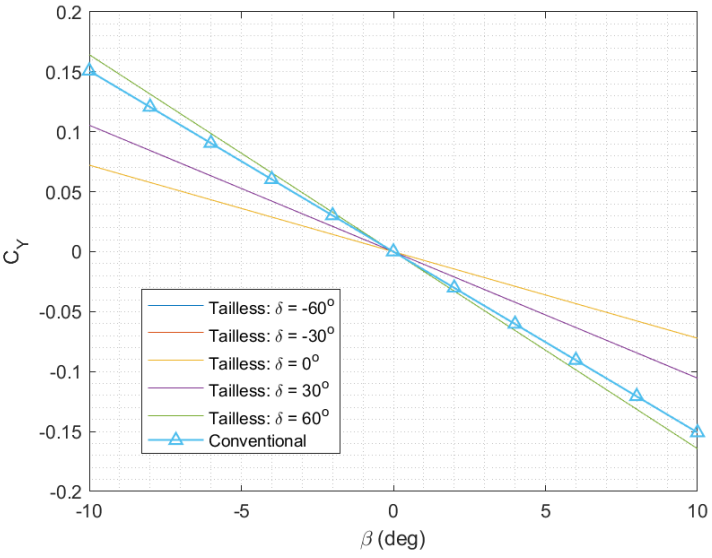

Figure 4.4: Side-force coefficient vs. Side-slip angle

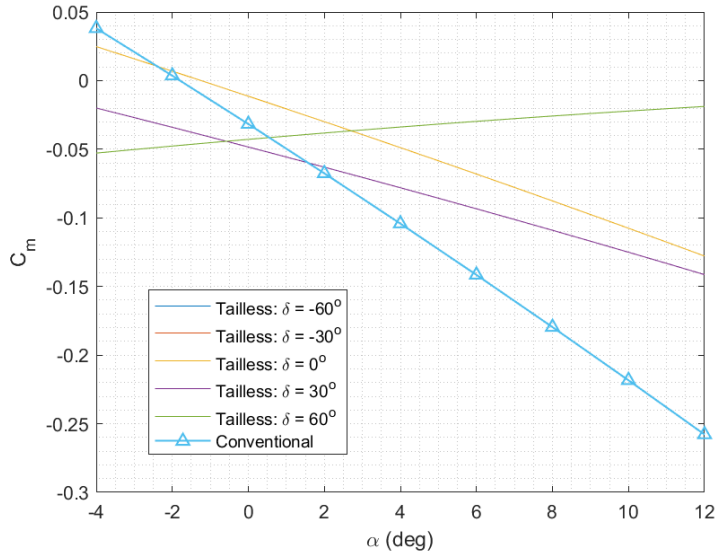

Figure 4.5: Pitch moment coefficient vs. Angle of attack

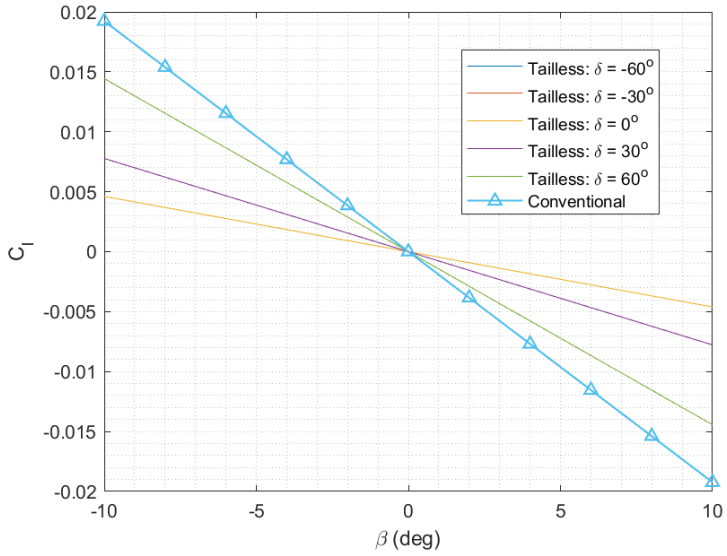

Figure 4.6: Roll moment coefficient vs. Sideslip angle

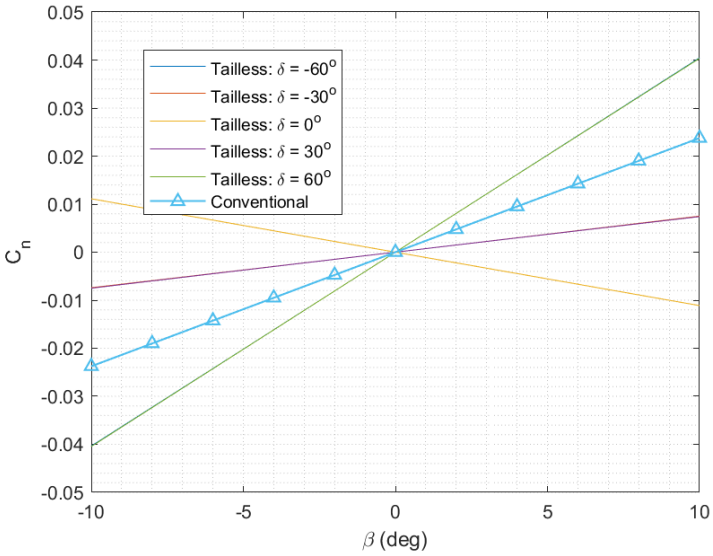

Figure 4.7: Yaw moment coefficient vs. Sideslip angle

4.3 Linear State Space Model of Vertical Tailless Aircraft

With the aerodynamic model we develop in section 4.1, the linear state space model of the vertical tailless aircraft is obtained using the same method we described in Chapter 2. The vertical tailless aircraft is trimmed at an altitude of 10000 ft (3048 m) and Mach number of 0.3. At the trim condition, the elevator deflection angle is $-2.5803°$, the engine throttle is 16.31%, the angle of attack are $4.8867°$. The rest of the control surface deflection angles are zero. Using MATLAB, the longitudinal 4th-order stability axes equation of motion is

calculated as

$$\frac{d}{dt}\begin{bmatrix} V \\ \gamma \\ q \\ \alpha \end{bmatrix} = \begin{bmatrix} -0.0134 & -9.8067 & -0.1955 & -12.3071 \\ 0.0020 & 0.0000 & 0.0218 & 0.9709 \\ -0.0000 & 0 & -1.6177 & -5.7292 \\ -0.0020 & -0.0000 & 0.9782 & -0.9709 \end{bmatrix} \begin{bmatrix} V \\ \gamma \\ q \\ \alpha \end{bmatrix} + \begin{bmatrix} 0.2055 & 4.0755 \\ 8.9456 & 0 \\ -13.3125 & 0 \\ -8.9456 & 0 \end{bmatrix} \begin{bmatrix} dE \\ dT \end{bmatrix} \tag{4.11}$$

where **V** is airspeed, $\boldsymbol{\gamma}$ is flight path angle, **q** is pitch rate, $\boldsymbol{\alpha}$ is angle of attack, **dE** is elevator deflection angle, **dT** is engine throttle.

The matrix associates with the state vector is the state matrix and the matrix relates to the control vector is the control matrix. From the state matrix, the eigenvalues and the eigenvectors of the matrix can be calculated.

The eigenvalues/poles of the longitudinal model are

$$\lambda_{1,2} = -0.0035 \pm 0.1254j \tag{4.12}$$

$$\lambda_{3,4} = -1.2975 \pm 2.3425j \tag{4.13}$$

The first and second eigenvalue correspond to the short-period mode. The third and fourth eigenvalue correspond to the phugoid mode. The natural frequency, damping ratio, and the period of each mode is calculated from the eigenvalues. It is observed that both

short-period mode and phugiod mode are underdamped and stable.

$$\omega_{ph} = 0.12547 rad/s \tag{4.14}$$

$$T_{ph} = 50.0754 s \tag{4.15}$$

$$\zeta_{ph} = 0.027631 \tag{4.16}$$

$$\omega_{sp} = 2.6778 rad/s \tag{4.17}$$

$$T_{sp} = 2.3464 s \tag{4.18}$$

$$\zeta_{sp} = 0.48454 \tag{4.19}$$

Comparing to the conventional version, the vertical tailless version has a greater damping ratio on the short-period mode and a smaller damping ratio on the phugoid mode.

The lateral/directional 4th-order stability axes equation of motion is calculated as

$$\begin{aligned} \frac{d}{dt}\begin{bmatrix} r \\ \beta \\ p \\ \phi \end{bmatrix} &= \begin{bmatrix} -0.1069 & -1.7246 & 0.1147 & 0 \\ -0.9981 & -0.0793 & 0.0001 & 0.0992 \\ 0.1501 & -2.3074 & -1.4278 & 0 \\ 0 & 0 & 1.0036 & 0 \end{bmatrix}\begin{bmatrix} r \\ \beta \\ p \\ \phi \end{bmatrix} \\ &+ \begin{bmatrix} 0.0942 & 0.6185 \\ -0.1184 & -0.6816 \\ -9.7723 & -0.1058 \\ 0 & 0 \end{bmatrix}\begin{bmatrix} dA \\ dTR \end{bmatrix} \end{aligned} \tag{4.20}$$

where **r** is yaw rate, $\boldsymbol{\beta}$ is sideslip angle, **p** is roll rate, $\boldsymbol{\phi}$ is bank angle, **dA** is aileron deflection angle, **dTR** is tail rotational angle.

The eigenvalues of the lateral/directional model are calculated as

$$\lambda_1 = 1.2211 \tag{4.21}$$

$$\lambda_2 = 0.0201 \tag{4.22}$$

$$\lambda_{3,4} = -1.4276 \pm 0.1321 j \tag{4.23}$$

The first eigenvalue corresponds to the spiral mode. The second eigenvalue correspond to the Dutch roll mode. The third and fourth eigenvalue correspond to the roll mode. It is shown that the spiral mode and Dutch roll mode are unstable. The roll mode becomes fast and stable but oscillatory.

The time constant natural frequencies, periods, and damping ratios of these modes are calculated as

$$\tau_{spiral} = 0.81892s \tag{4.24}$$

$$\tau_{Dutchroll} = 49.8737s \tag{4.25}$$

$$\omega_{roll} = 1.4337\text{rad/s} \tag{4.26}$$

$$T_{roll} = 4.3825s \tag{4.27}$$

$$\zeta_{roll} = 0.99574 \tag{4.28}$$

Comparing to the conventional aircraft, the vertical tailless version lose stability in all three modes due to the removal of vertical tail.

4.4 Controllability and Observability

Before moving on to controller design, we need to check the controllability of the system. The controllability matrix is defined as Eq. 4.29.

$$\mathcal{C} = \begin{bmatrix} A & AB & A^2B & ... & A^{n-1}B \end{bmatrix} \tag{4.29}$$

Substituting the state matrix A and the input matrix B from Eq. 4.20 into Eq. 4.29, the controllability matrix is obtained as Eq. 4.30

$$\begin{bmatrix} 0.0942 & 0.6185 & -0.9272 & 1.0973 & 1.8811 & 1.0624 & -2.4603 & 1.5862 \\ -0.1184 & -0.6816 & -0.08579 & -0.5632 & -0.0390 & -1.0608 & -0.4592 & -0.7955 \\ -9.7723 & -0.1058 & 14.2404 & 1.8166 & -20.2737 & -1.1295 & 29.3192 & 4.2198 \\ 0 & 0 & -9.8080 & -0.1061 & 14.2923 & 1.8232 & -20.3477 & -1.1336 \end{bmatrix} \tag{4.30}$$

It is observed that the controllability matrix has full row rank (rank($\mathcal{C}$)=4). Thus, the system is controllable, which means we can drive any initial conditions to the desired states within a finite time interval by using proper inputs.

Similarly, the observability matrix is defined as Eq. 4.31.

$$\mathcal{CO} = \begin{bmatrix} C \\ CA \\ CA^2 \\ ... \\ CA^{n-1} \end{bmatrix} \tag{4.31}$$

Substituting the state matrix A and the output matrix C ($I_{4\times4}$) from Eq. 4.20 into Eq. 4.31, the observability matrix is obtained as Eq. 4.32

$$\mathcal{CO} = \begin{bmatrix} 1 & 0 & 0 & 0 \\ 0 & 1 & 0 & 0 \\ 0 & 0 & 1 & 0 \\ 0 & 0 & 0 & 1 \\ -0.1069 & -1.7246 & 0.1147 & 0 \\ -0.9981 & -0.07932 & 0.0001182 & 0.09919 \\ 0.1501 & -2.3074 & -1.428 & 0 \\ 0 & 0 & 1.004 & 0 \\ 1.7499 & 0.05643 & -0.1763 & -0.1711 \\ 0.1859 & 1.7273 & -0.01515 & -0.007867 \\ 2.0726 & 3.2187 & 2.0556 & -0.2289 \\ 0.1506 & -2.3158 & -1.4330 & 0 \\ -0.2699 & -2.6156 & 0.2809 & 0.005597 \\ -1.7461 & -0.4226 & 0.03528 & 0.1713 \\ -3.1256 & -8.5728 & -2.9265 & 0.3193 \\ 2.0802 & 3.2305 & 2.0631 & -0.2297 \end{bmatrix} \tag{4.32}$$

It is shown that the observability matrix has full column rank (rank($\mathcal{CO}$)=4). Therefore the system is observable, which means we can determine the states of the system at any given time from the output measurements including the initial conditions.

4.5 LQR Design for Lateral/Directional Dynamics

It is observed in the previous section that there exists two unstable modes in lateral/directional dynamics. When the aircraft is conducting steady level flight, any disturbance on lateral/directional states (sideslip angle, bank angle, roll rate, yaw rate) or inputs (aileron, tail, spoiler) would make the aircraft unstable. Since the vertical tailless aircraft can't regain lateral stability on its own, a feedback controller is designed to compensate the instability.

The controller we design is a linear quadratic regulator (LQR) which was first introduced by R. E. Kalman in 1960s. For any linear time invariant system in the form of Eq. 4.33

$$\dot{x}(t) = Ax(t) + Bu(t) \tag{4.33}$$

The performance measure of a time invariant LQR is defined as

$$J = \int_0^\infty (x^T Q x + u^T R u) dt \tag{4.34}$$

The objective of minimizing performance measure is accomplished by minimizing states and inputs over time which eventually stabilizes the system. The Q and R matrices are weighting matrices. The diagonal terms of Q and R represents how much you want to penalize the state/input. The optimal state feedback gain is obtained by solving the following algebraic Riccati equation

$$0 = PA + A^T P - PBR^{-1}B^T P + Q \tag{4.35}$$

And the input is given as

$$u = -R^{-1}B^T P x \tag{4.36}$$

Given the lateral/direction model in Eq. 4.20, $Q = \begin{bmatrix} 1 & 0 & 0 & 0 \\ 0 & 1 & 0 & 0 \\ 0 & 0 & 1 & 0 \\ 0 & 0 & 0 & 1 \end{bmatrix}$, and $R = \begin{bmatrix} 1 & 0 \\ 0 & 1 \end{bmatrix}$, the

optimal state feedback gain K is calculated as

$$K = \begin{bmatrix} -0.0172 & 0.1651 & -0.9610 & -1.0016 \\ 1.8950 & -2.4265 & 0.0499 & -0.1177 \end{bmatrix} \tag{4.37}$$

The eigenvalues of the closed-loop system are

$$\lambda_1 = -9.8248 \tag{4.38}$$

$$\lambda_{2,3} = -1.4903 \pm 0.1677 \tag{4.39}$$

$$\lambda_4 = -0.9994 \tag{4.40}$$

The closed-loop lateral/directional modes are faster and better damped than that of the open-loop lateral/directional modes. The Dutch roll mode is back to oscillatory and the roll mode is now monotonic.

The closed-loop time response to initial perturbation of yaw rate, roll rate, sideslip angle, and bank angle are plotted as shown in Fig. 4.8. In Fig. 4.8a, the perturbations in yaw rate, roll rate, sideslip angle, and bank angle are critically damped out within six seconds. In Fig. 4.8b, the aileron deflection and tail rotation starts at about 0.30 rad and 0.16 rad are damped out within four seconds. For comparison, the open-loop time response to the same perturbations are plotted as shown in Fig. 4.9, the states of the system diverges without a controller as predicted.

In this chapter, we modeled the rigid body dynamics of a vertical tailless aircraft. We examined the longitudinal and lateral/direction stability of the vertical tailless aircraft and compared it to the conventional version. We also implemented a linear quadratic regulator for stability augmentation purpose. In the next chapter, we will analyze the aerodynamic data of a model aircraft from wind tunnel and calculate its drag coefficient reduction between conventional and vertical tailless model.

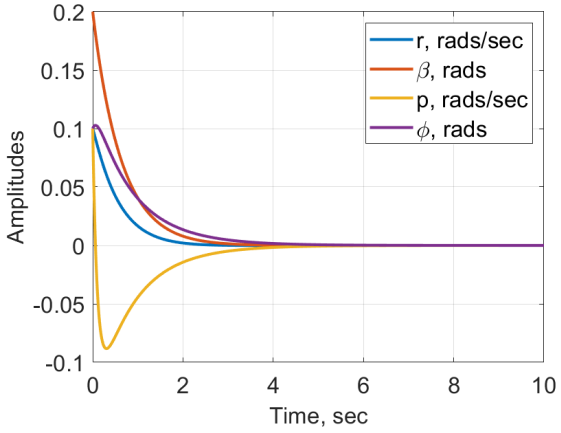

(a) Yaw rate, roll rate, sideslip angle, and bank angle

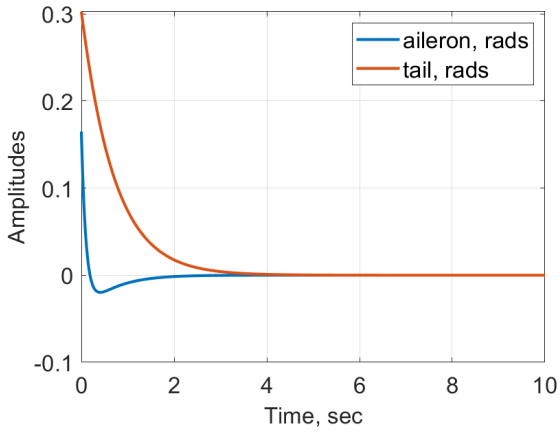

(b) Aileron angle, tail rotation angle

Figure 4.8: Closed-loop time response to initial perturbation of yaw rate, roll rate, sideslip angle, and bank angle. $\Delta r = 0.1$ rad/s, $\Delta p = 0.1$ rad, $\Delta\beta = 0.2$ rad, $\Delta\phi = 0.1$ rad/s

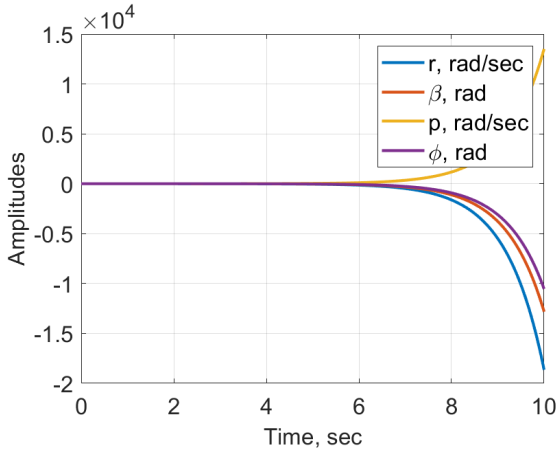

Figure 4.9: Open-loop time response to initial perturbation of yaw rate, roll rate, sideslip angle, and bank angle. $\Delta r = 0.1$ rad/s, $\Delta p = 0.1$ rad, $\Delta\beta = 0.2$ rad, $\Delta\phi = 0.1$ rad/s

Chapter 5

WIND TUNNEL DATA ANALYSIS

In this chapter, we analyze the aerodynamic data of a scaled RV-4 Aerobatics model which are collected in the Kirsten Wind Tunnel for both conventional and vertical tailless version. The data includes force and moment coefficients in terms of body-axis , stability-axis, and wind-axis. The angle of attack ranges from $-4°$ to $11°$. The side-slip angle is from $-10°$ to $10°$. The elevator deflects from $-14°$ to $28°$. The rudder deflects from $-20°$ to $0°$. The horizontal tail rotates from $0°$ to $90°$. In the first section, we present an overview of the aerodynamic coefficients and stability derivatives. Then we investigate several cases where the force and moments coefficients of the conventional and tailless aircraft are comparable and find the corresponding drag coefficient reduction.

5.1 Aerodynamic Force and Moment Coefficients

The aerodynamic coefficients of the conventional RV-4 model are plotted as shown in Fig. 5.1-5.6. It is observed that C_{m_α} and C_{l_β} are negative. C_{n_β} is positive. As a result, the conventional RV-4 model is guaranteed to have static longitudinal stability and lateral/directional stability.

The aerodynamic force and moment coefficients for the vertical tailless model are plotted as shown in Fig. 5.7-5.12. The lift coefficient and drag coefficient varies slightly at different tail rotation angles. As the tail rotation angle increases, the side force curve slope C_{Y_β} increases and remains negative, the pitch moment curve slope C_{m_α} decreases and remains negative, the roll moment curve slope C_{l_β} increases and remains negative, the yaw moment curve slope C_{n_β} increases and remains positive. Comparing to the simulated data in Chapter 4, the effect of rotary tail on static stability follows the same trend.

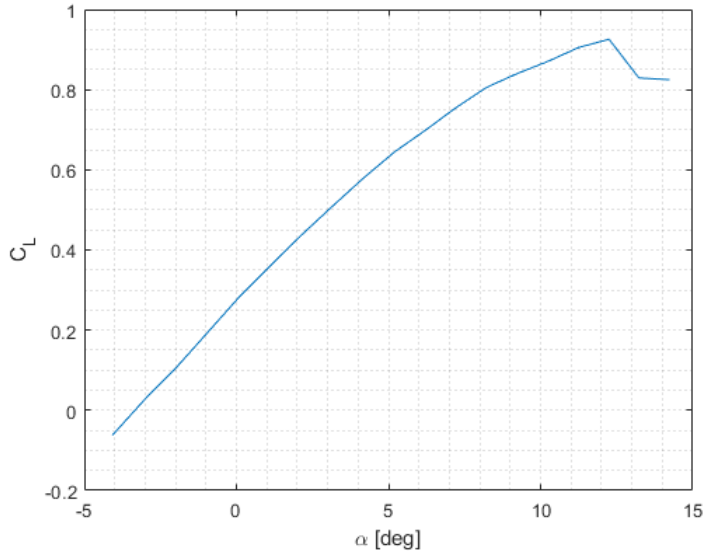

Figure 5.1: Lift Coefficient vs. Angle of Attack

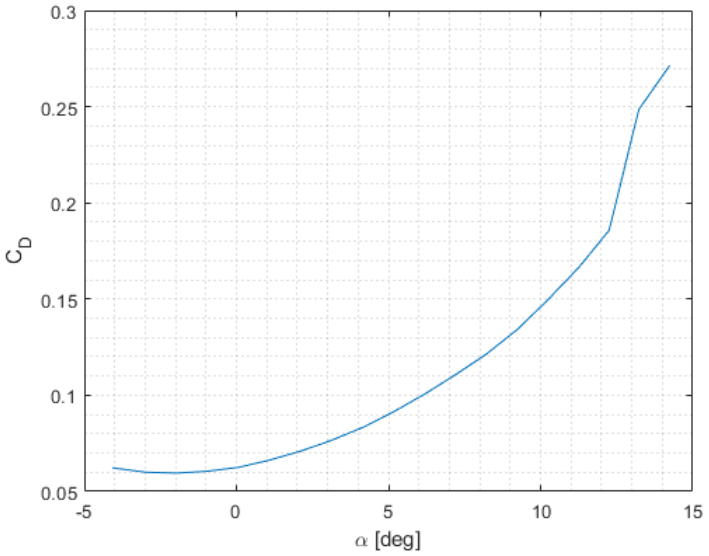

Figure 5.2: Drag Coefficient vs. Angle of Attack

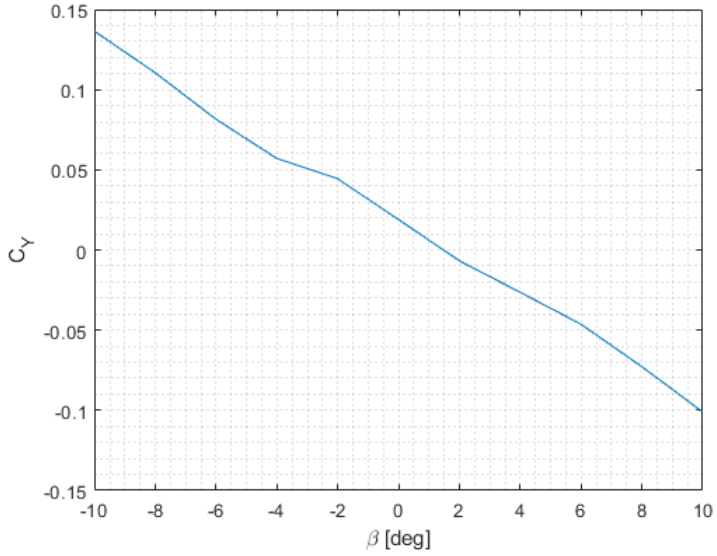

Figure 5.3: Side Force Coefficient vs. Side-slip Angle

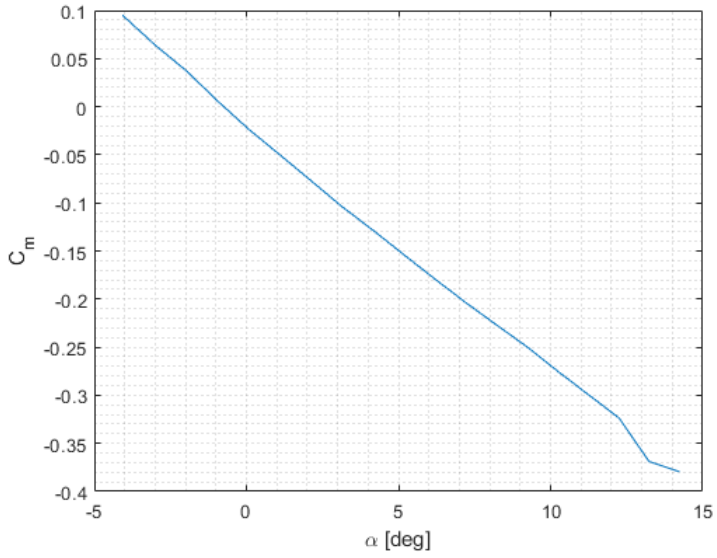

Figure 5.4: Pitch Moment Coefficient vs. Angle of Attack

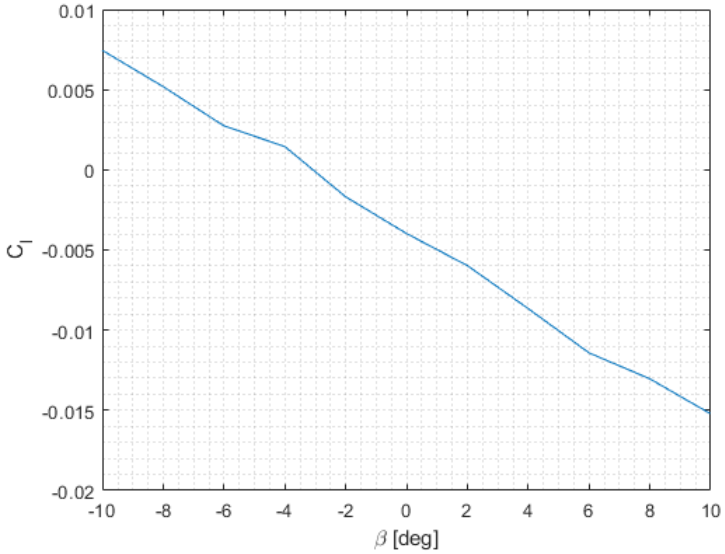

Figure 5.5: Roll Moment Coefficient vs. Side-slip Angle

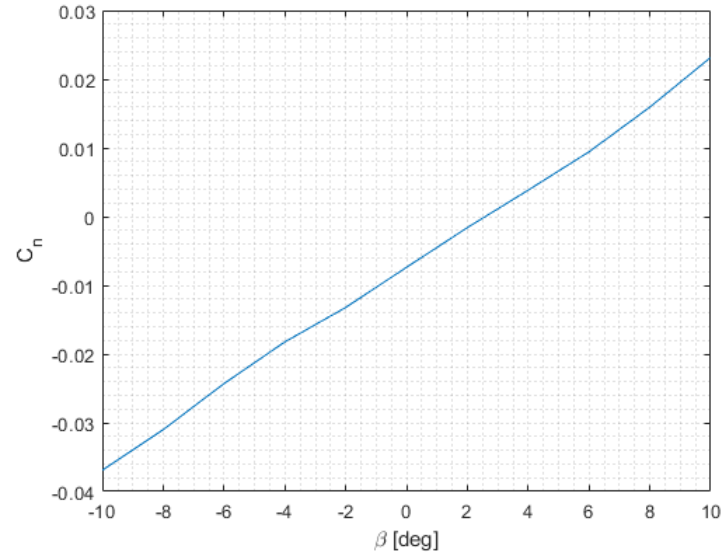

Figure 5.6: Yaw Moment Coefficient vs. Side-slip Angle

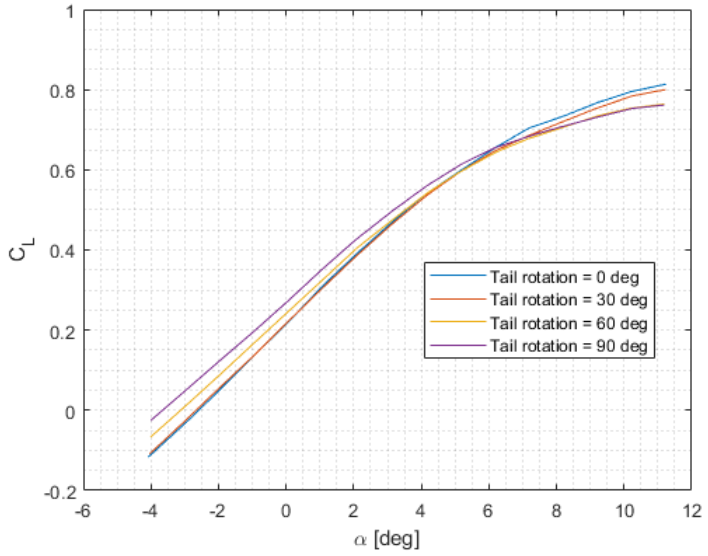

Figure 5.7: Lift Coefficient vs. Angle of Attack

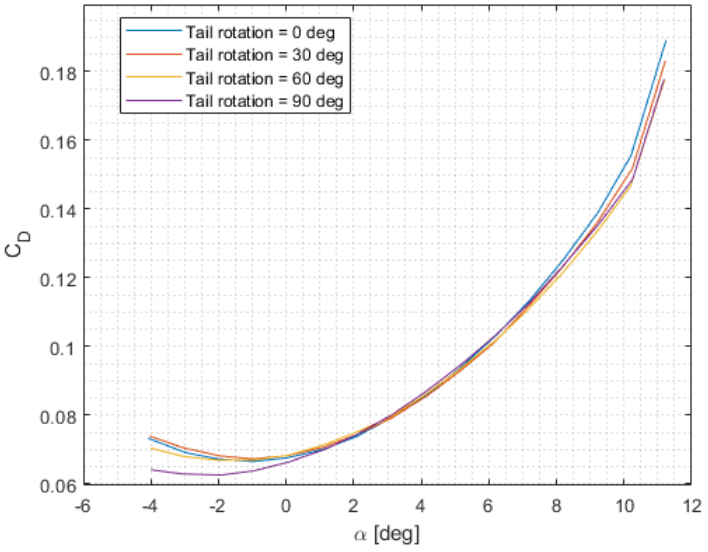

Figure 5.8: Drag Coefficient vs. Angle of Attack

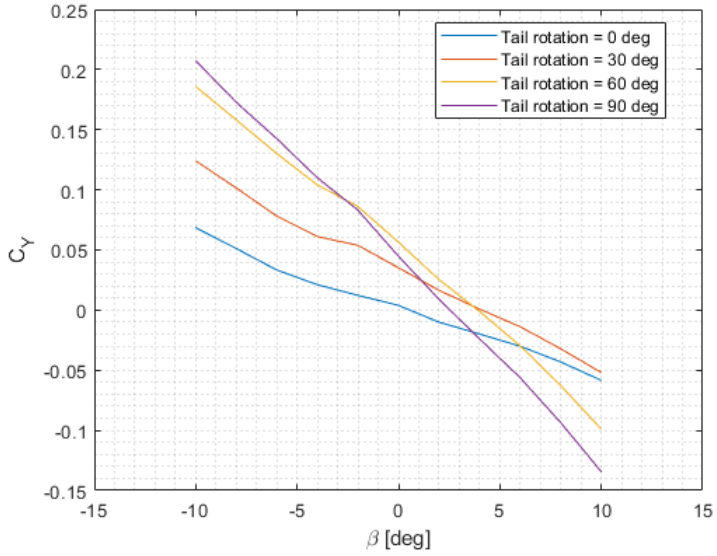

Figure 5.9: Side Force Coefficient vs. Side-slip Angle

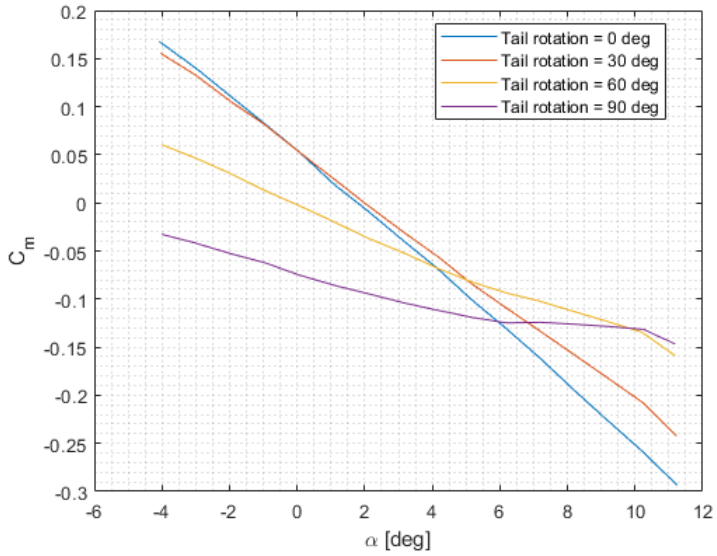

Figure 5.10: Pitch Moment Coefficient vs. Angle of Attack

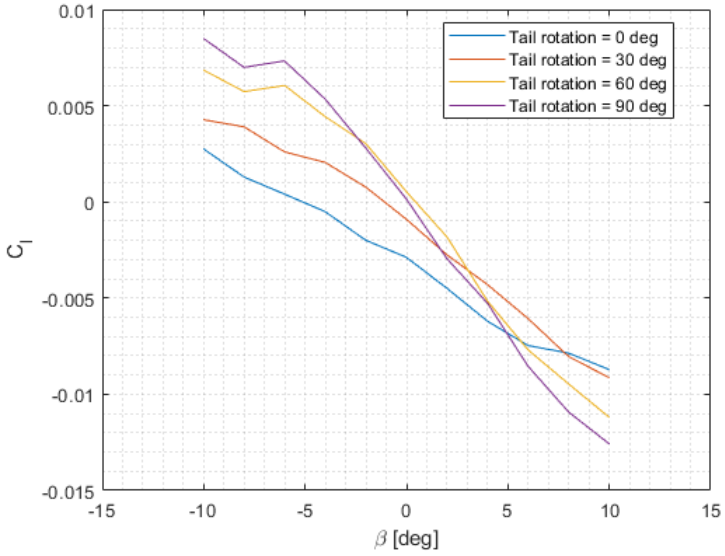

Figure 5.11: Roll Moment Coefficient vs. Side-slip Angle

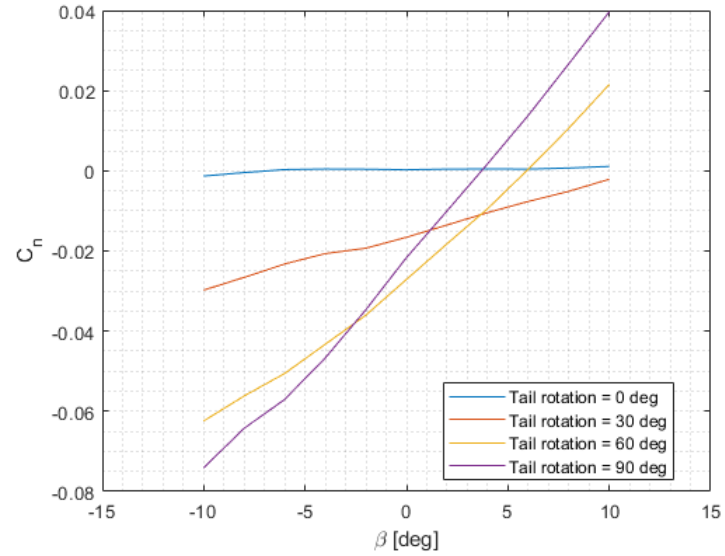

Figure 5.12: Yaw Moment Coefficient vs. Side-slip Angle

5.2 Stability Derivatives

The stability derivatives are defined as the rate of change of rolling/yawing/pitching moment with respect to sideslip angle/angle of attack. For conventional RV-4 model, the longitudinal stability derivative/pitch stiffness C_{M_α} is plotted in Fig. 5.13, the yaw stiffness C_{N_β} is plotted in Fig. 5.14, the roll stiffness C_{l_β} is plotted in Fig. 5.15. The mean $C_{M_\alpha} = -1.4775$ per radian, the mean $C_{N_\beta} = 0.16841$ per radian, the mean $C_{l_\beta} = -0.066949$ per radian. As for vertical tailless RV-4 model, the longitudinal stability derivative/pitch stiffness C_{M_α} is plotted in Fig. 5.13, the yaw stiffness C_{N_β} is plotted in Fig. 5.14, the roll stiffness C_{l_β} is plotted in Fig. 5.15. The average roll/pitch/yaw stiffness of the conventional and tailless RV-4 model are tabulated in Table. 5.1.

5.2.1 Stability Derivatives of Conventional RV-4 Model

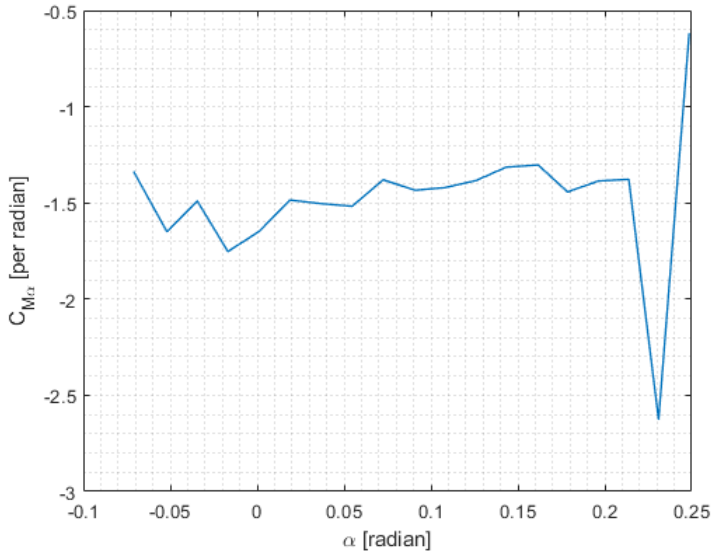

Figure 5.13: Pitch Stiffness vs. Angle of Attack

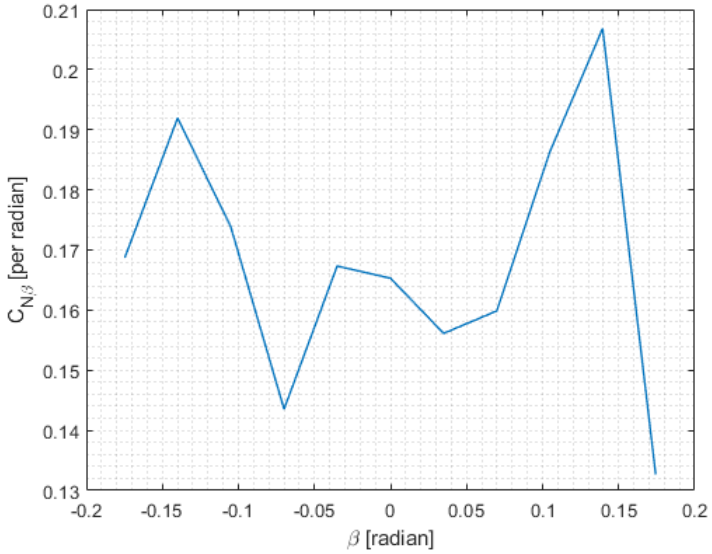

Figure 5.14: Yaw Stiffness vs. Side-slip Angle

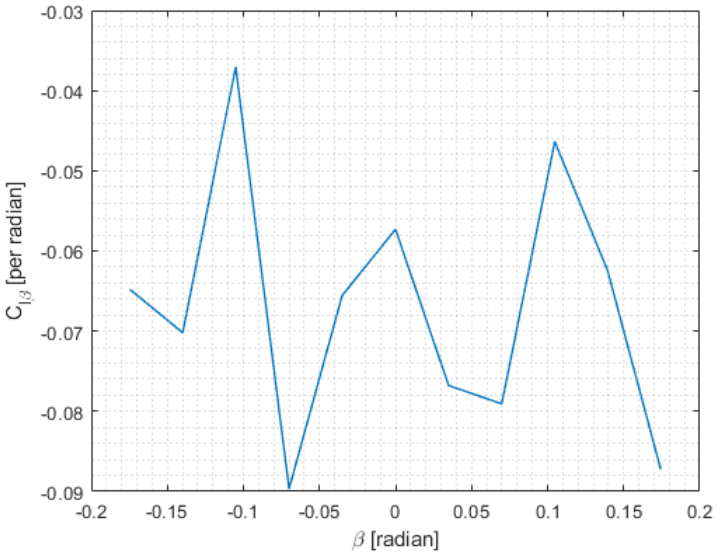

Figure 5.15: Roll Stiffness vs. Side-slip Angle

5.2.2 Stability Derivatives of Vertical Tailless RV-4 Model

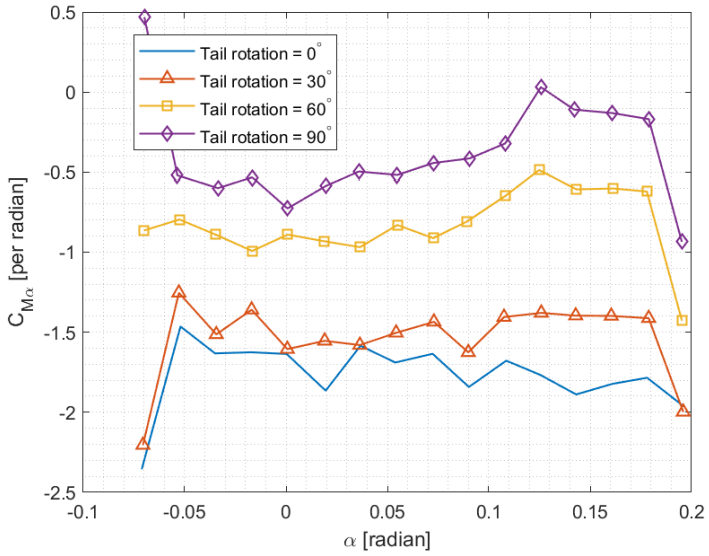

Figure 5.16: Pitch Stiffness vs. Angle of Attack

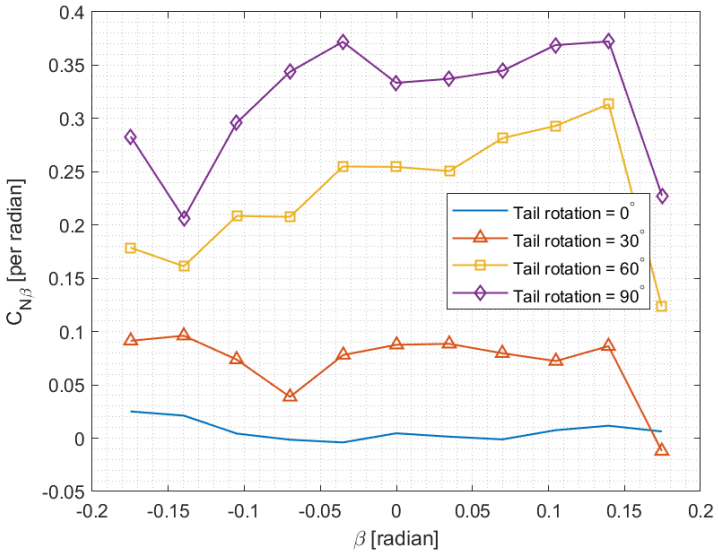

Figure 5.17: Yaw Stiffness vs. Side-slip Angle

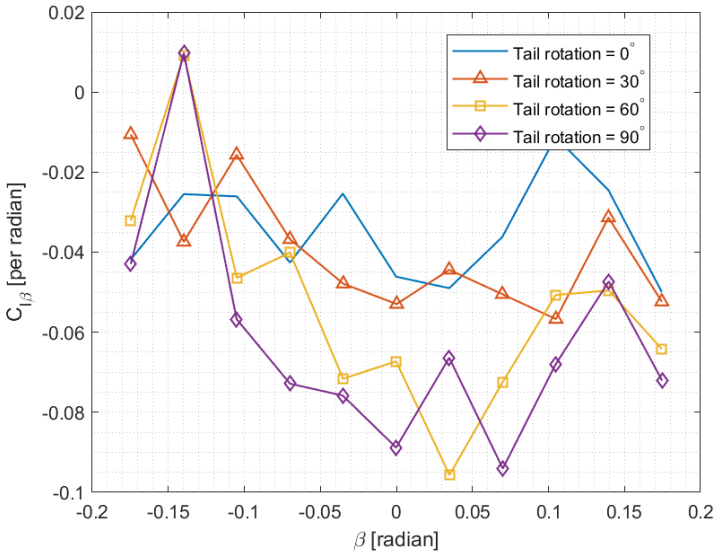

Figure 5.18: Roll Stiffness vs. Side-slip Angle

Table 5.1: Average Stability Derivatives of Conventional and Vertical Tailless RV-4 Model

	Conventional	Vertical Tailless			
		$\delta_h = 0°$	$\delta_h = 30°$	$\delta_h = 60°$	$\delta_h = 90°$
C_{M_α} per radian	-1.4775	-1.7645	-1.5389	-0.82989	-0.37531
C_{N_β} per radian	0.16841	0.0068639	0.070985	0.22982	0.31685
C_{l_β} per radian	-0.066949	-0.034406	-0.039696	-0.052812	-0.061392

5.3 Drag Coefficient Reduction During Steady Level Flight

For steady level flight, the total lift of the aircraft equals to the gross weight, the drag equals to the thrust. the roll, pitch, and yaw moments are zero so that the aircraft is trimmed. Given the conditions listed above, an optimization problem is formulated as shown in Eq. 5.1 to find the corresponding angle of attack and control surface deflections angles. Fig. 5.19 shows that the drag coefficient of the conventional RV-4 model is greater than its vertical

tailless version. The percentage drag coefficient reduction is calculated using Eq. 5.3 and plotted as shown in Fig. 5.20. The average drag coefficient reduction is 3.18%. The control surface deflection angles for both cases are plotted as Fig. 5.21 and Fig. 5.22. It is observed that the rudder deflection angle and tail rotation angle are fixed at zero degrees. The elevator deflection angle in both cases are different because the angle of attack are different in shown in Fig. 5.23. The force and moment coefficient matchness are plotted from Fig. 5.24 to Fig. 5.28. It is observed that the lift coefficient, pitch moment coefficient and roll moment coefficient match well. As for yaw moment coefficient and side force coefficient, their order of magnitude are small enough for the case to be consider comparable.

$$\begin{aligned} \min_{\alpha,\beta,\delta_e,\delta_{r/h}} \quad & |C_M(\alpha,\beta,\delta_e,\delta_{r/h})| + |C_N(\alpha,\beta,\delta_e,\delta_{r/h})| + |C_R(\alpha,\beta,\delta_e,\delta_{r/h})| \\ & + |C_Y(\alpha,\beta,\delta_e,\delta_{r/h})| + |C_L(\alpha,\beta,\delta_e,\delta_{r/h}) - C_L^*| \\ \text{s.t.} \quad & -3^\circ \leq \alpha \leq 11^\circ \\ & \beta = \delta_{r/h} = 0^\circ \\ & -14^\circ \leq \delta_e \leq 20^\circ \end{aligned} \tag{5.1}$$

$$C_L^* = \frac{W}{\frac{1}{2}\rho V^2 S} \tag{5.2}$$

$$\text{Drag Coefficient Reduction} = \frac{C_{D_{CONVENTIONAL}} - C_{D_{TAILLESS}}}{C_{D_{CONVENTIONAL}}} \times 100 \tag{5.3}$$

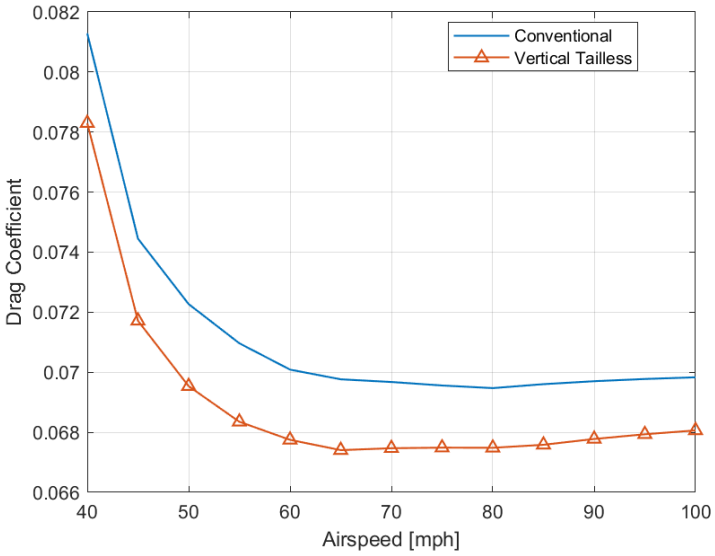

Figure 5.19: Drag Coefficient vs Airspeed

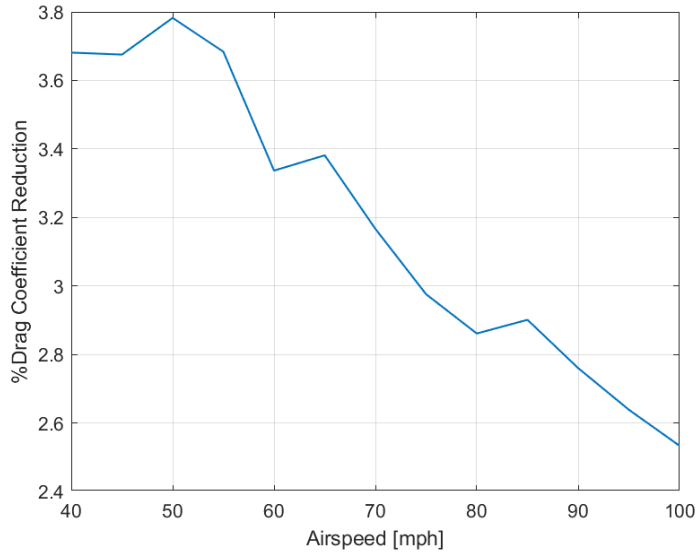

Figure 5.20: Percentage Drag Coefficient Reduction vs Airspeed

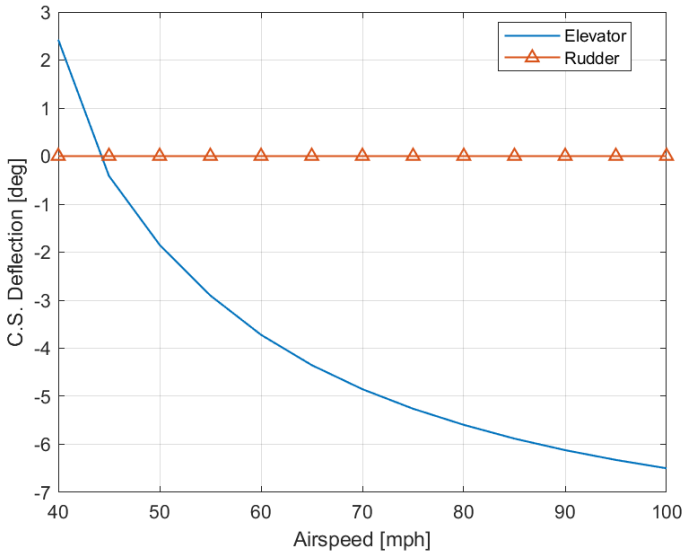

Figure 5.21: Control Surface Deflection vs Airspeed

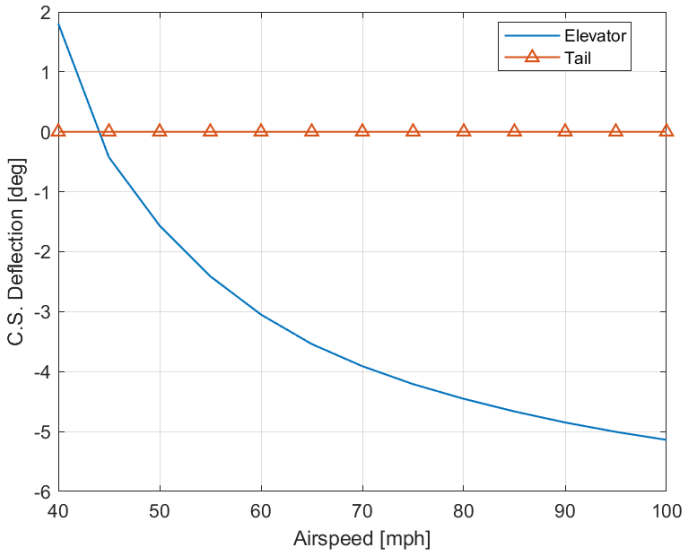

Figure 5.22: Control Surface Deflection vs Airspeed

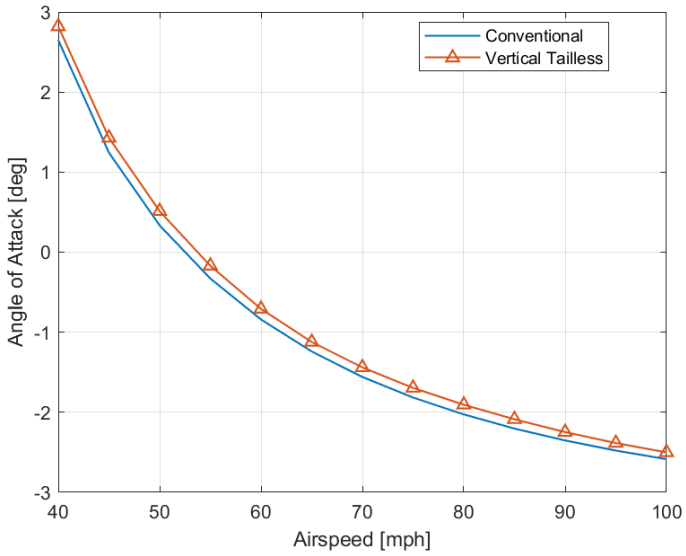

Figure 5.23: Angle of Attack vs Airspeed

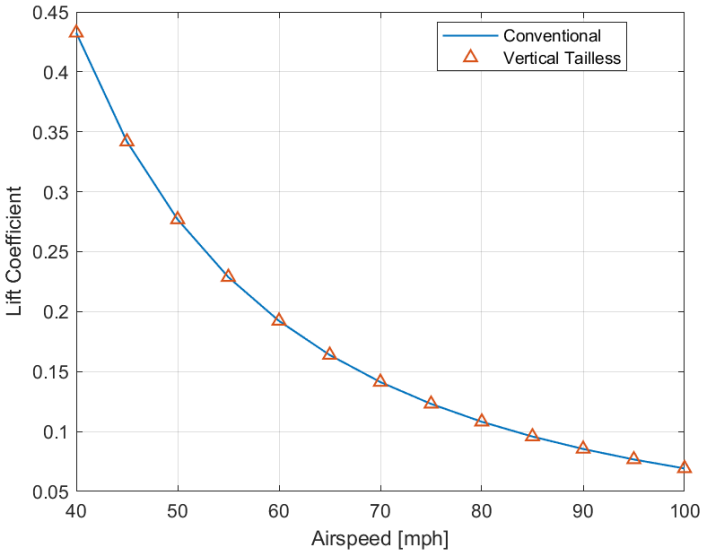

Figure 5.24: Lift Coefficient vs Airspeed

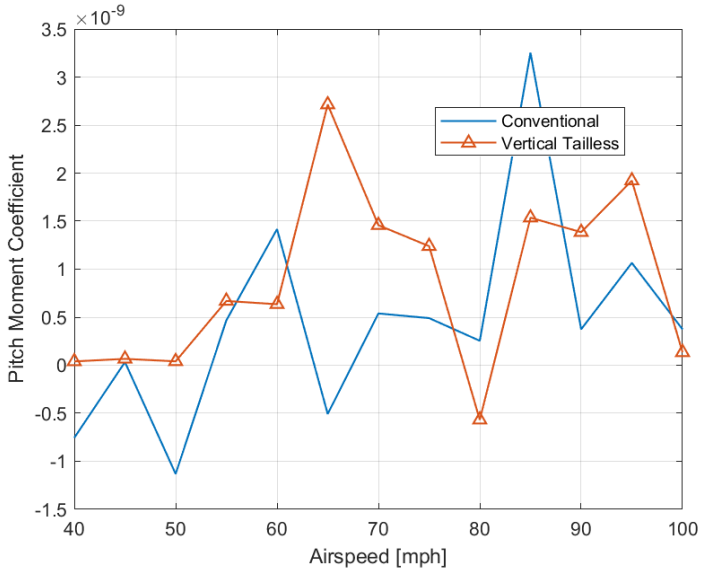

Figure 5.25: Pitch Moment Coefficient vs Airspeed

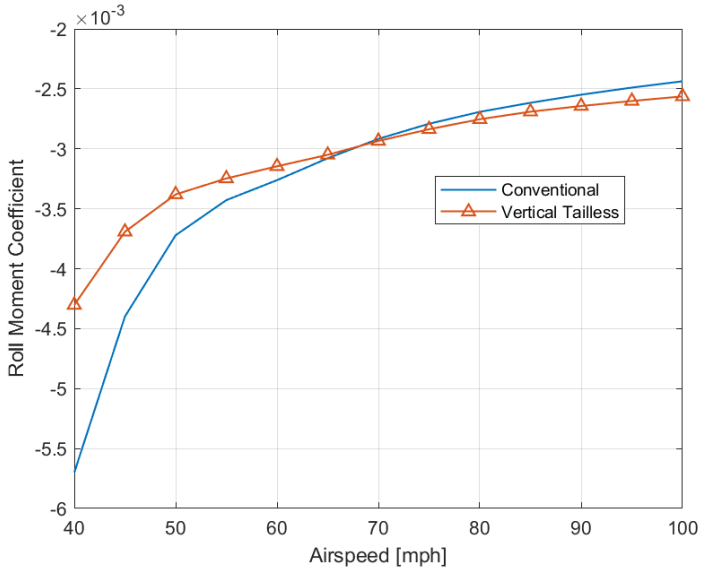

Figure 5.26: Roll Moment Coefficient vs Airspeed

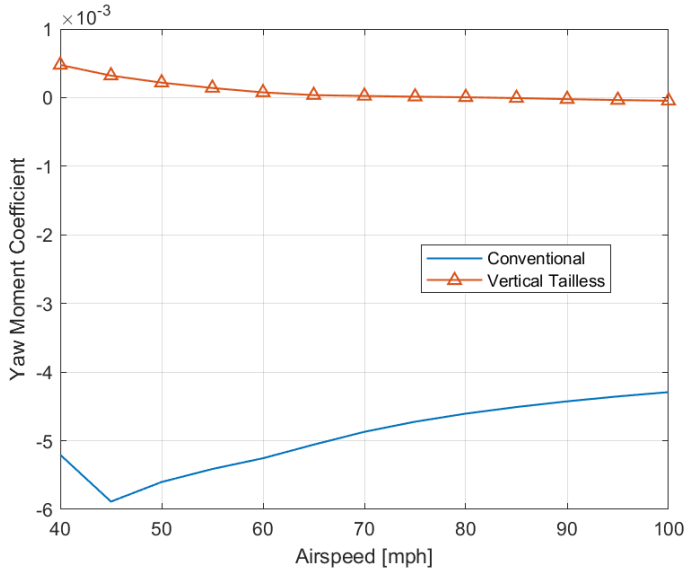

Figure 5.27: Yaw Moment Coefficient vs Airspeed

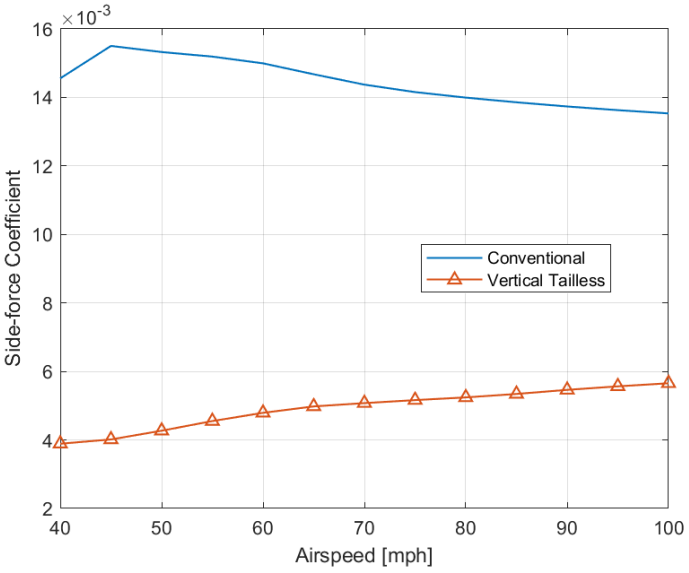

Figure 5.28: Side-force Coefficient vs Airspeed

5.4 Drag Coefficient Reduction During Steady Level Turn

The second case is steady level turn which is essentially steady level flight with a fixed banking angle of 30°. For steady level turn, the total lift of the aircraft is equal to the gross weight divided by the cosine of banking angle, the drag equals to the thrust. the roll, pitch, and yaw moments are zero so that the aircraft is trimmed. With the conditions listed above, the corresponding angle of attack and control surface deflections angles are found for various airspeed. Fig. 5.29 shows that the drag coefficient of the conventional RV-4 model is greater than its vertical tailless version. The percentage drag coefficient reduction is calculated using Eq. 5.3 and plotted as shown in Fig. 5.30. The average drag coefficient reduction is 3.25%. The control surface deflection angles for both cases are plotted as Fig. 5.31 and Fig. 5.32. It is observed that the rudder deflection angle and tail rotation angle are fixed at zero degrees. The elevator deflection angle in both cases are different because the angle of attack are different in shown in Fig. 5.33. The force and moment coefficient matchness are plotted from Fig. 5.34 to Fig. 5.38. It observed that the lift coefficient, pitch moment coefficient and roll moment coefficient match well. The matchness of these curves describes how comparable these two cases are.

$$
\begin{aligned}
\min_{\alpha,\beta,\delta_e,\delta_{r/h}} \quad & |C_M(\alpha,\beta,\delta_e,\delta_{r/h})| + |C_N(\alpha,\beta,\delta_e,\delta_{r/h})| + |C_R(\alpha,\beta,\delta_e,\delta_{r/h})| \\
& + |C_Y(\alpha,\beta,\delta_e,\delta_{r/h})| + |C_L(\alpha,\beta,\delta_e,\delta_{r/h}) - C_L^*| \\
\text{s.t.} \quad & -3^\circ \leq \alpha \leq 11^\circ \\
& \beta = \delta_{r/h} = 0^\circ \\
& -14^\circ \leq \delta_e \leq 20^\circ \\
& \phi = 30^\circ
\end{aligned}
\tag{5.4}
$$

$$
C_L^* = \frac{W}{\frac{1}{2}\rho V^2 S \cos\phi} \tag{5.5}
$$

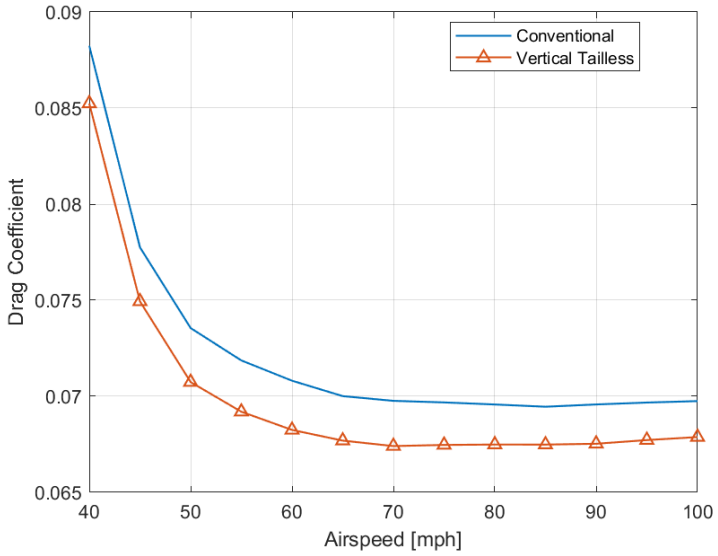

Figure 5.29: Drag Coefficient vs Airspeed

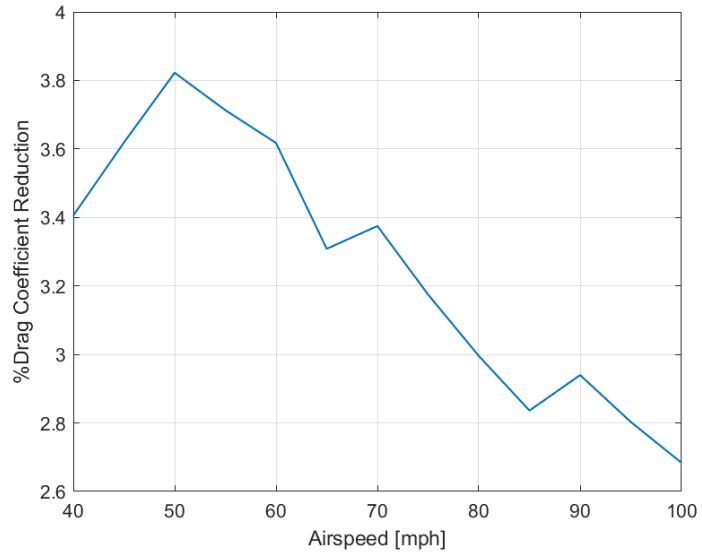

Figure 5.30: Percentage Drag Coefficient Reduction vs Airspeed

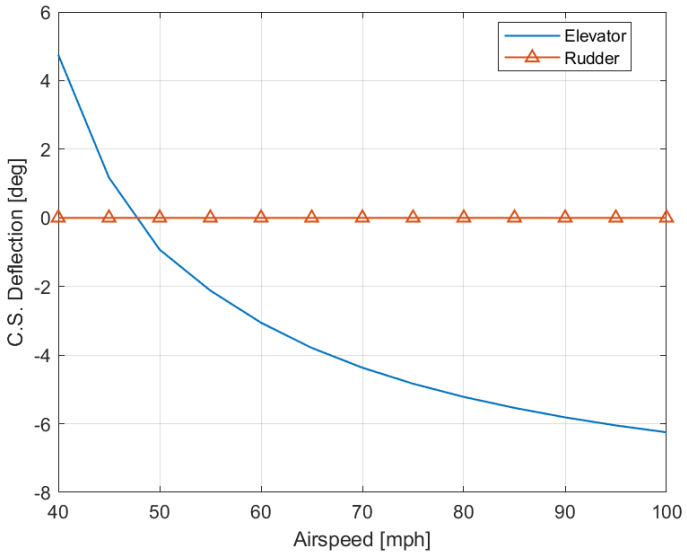

Figure 5.31: Control Surface Deflection vs Airspeed

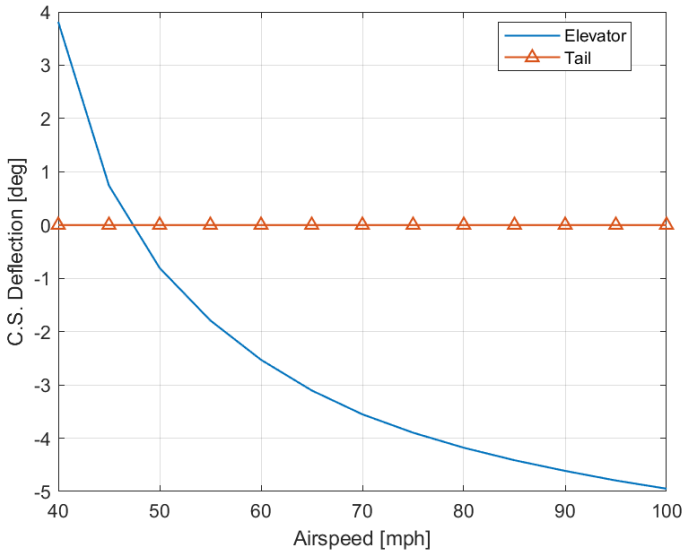

Figure 5.32: Control Surface Deflection vs Airspeed

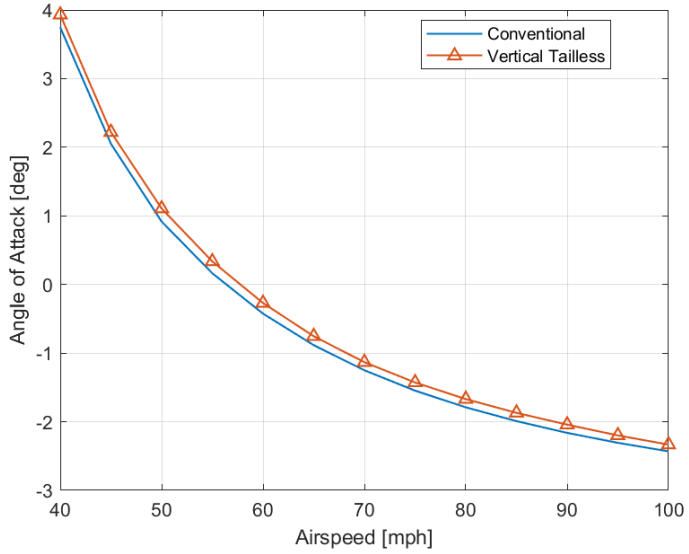

Figure 5.33: Angle of Attack vs Airspeed

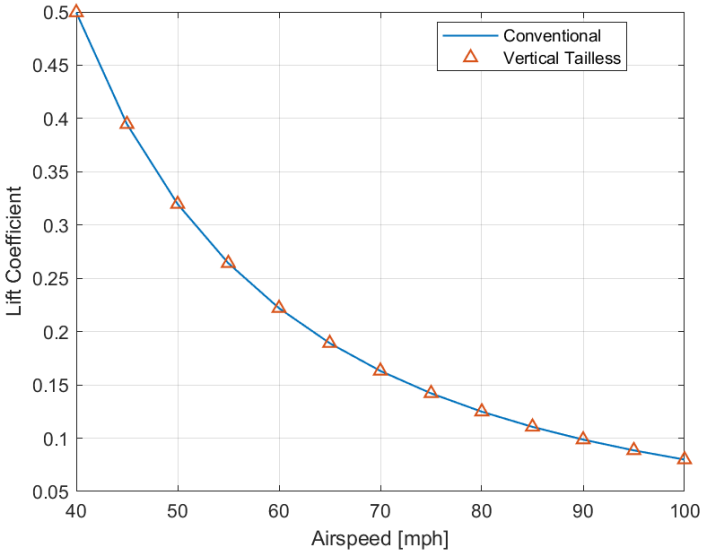

Figure 5.34: Lift Coefficient vs Airspeed

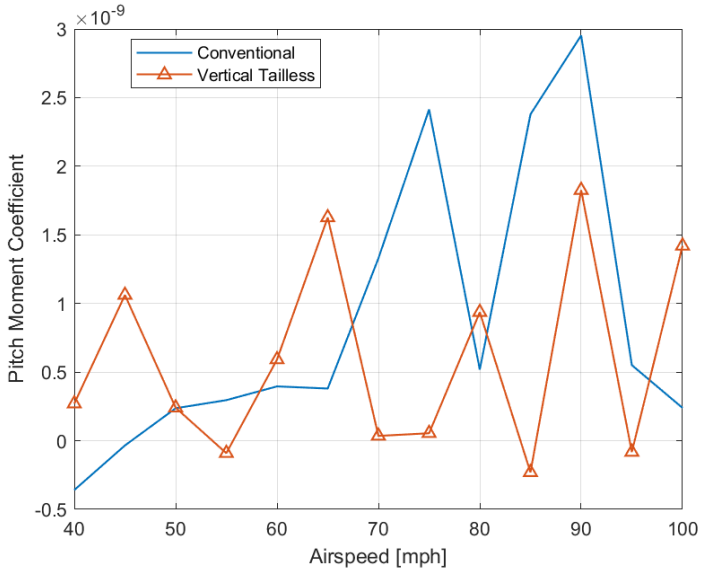

Figure 5.35: Pitch Moment Coefficient vs Airspeed

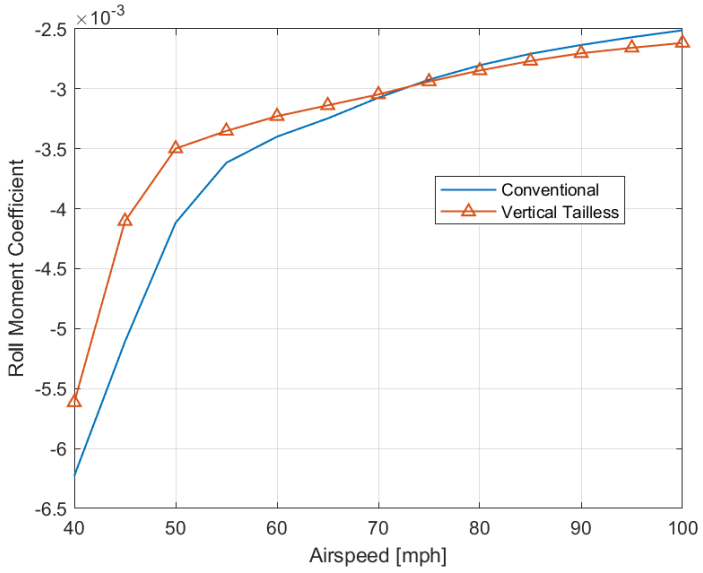

Figure 5.36: Roll Moment Coefficient vs Airspeed

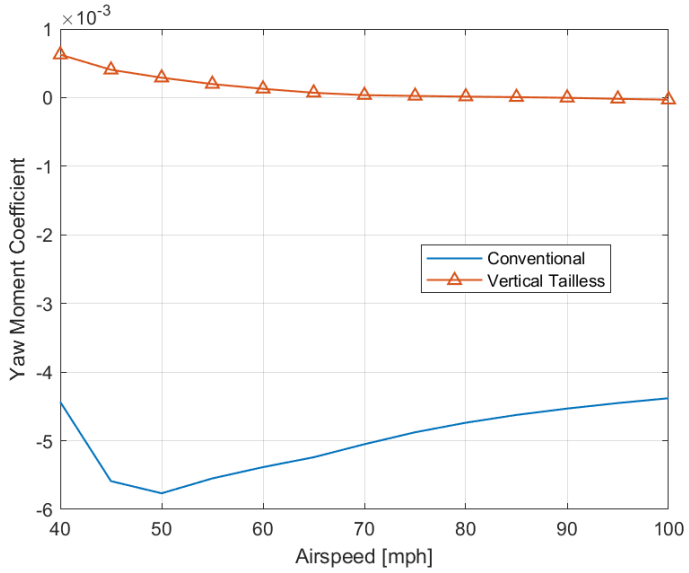

Figure 5.37: Yaw Moment Coefficient vs Airspeed

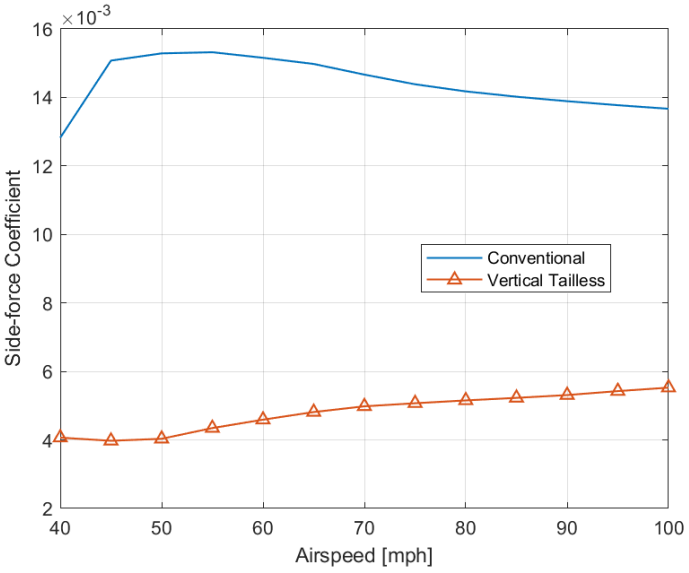

Figure 5.38: Side-force Coefficient vs Airspeed

5.5 Drag Coefficient Reduction at Fixed Elevator and Rudder Deflection Angles

For the third case, we investigate the drag coefficient reduction at selected control surface deflection angles. First we calculate the force and moment coefficients of the conventional RV-4 model. Then, to match with these coefficients, we find the corresponding angle of attack and control surface deflections angles for the tailless RV-4 model using the algorithm summarized in Eq. 5.6. The matching curve of the force and moment coefficients plotted in Fig. 5.42 to Fig. 5.46 show that the two cases are generally comparable. Fig. 5.39 shows that the drag coefficient of the conventional RV-4 model is greater than its vertical tailless version. The percentage drag coefficient reduction is calculated using Eq. 5.3 and plotted as shown in Fig. 5.40. When $\beta = 10^\circ$, $\delta_E = 20^\circ$, $\delta_R = -4^\circ$, the average drag coefficient reduction is about 10.4%. The control surface deflection angles for the tailless model are plotted as Fig. 5.41.

$$
\begin{aligned}
\min_{\alpha,\beta,\delta_e,\delta_h} \quad & |C_{M_{conventional}}(\alpha,\beta,\delta_e,\delta_r) - C_{M_{tailless}}(\alpha,\beta,\delta_e,\delta_h)| \\
& + |C_{N_{conventional}}(\alpha,\beta,\delta_e,\delta_r) - C_{N_{tailless}}(\alpha,\beta,\delta_e,\delta_h)| \\
& + |C_{R_{conventional}}(\alpha,\beta,\delta_e,\delta_r) - C_{R_{tailless}}(\alpha,\beta,\delta_e,\delta_h)| \\
& + |C_{Y_{conventional}}(\alpha,\beta,\delta_e,\delta_r) - C_{Y_{tailless}}(\alpha,\beta,\delta_e,\delta_h)| \\
& + |C_{L_{conventional}}(\alpha,\beta,\delta_e,\delta_r) - C_{L_{tailless}}(\alpha,\beta,\delta_e,\delta_h)| \\
\text{s.t.} \quad & -3^\circ \leq \alpha \leq 11^\circ \\
& -10^\circ \leq \beta \leq 10^\circ \\
& -14^\circ \leq \delta_e \leq 20^\circ \\
& -20^\circ \leq \delta_r \leq 0^\circ \\
& 0^\circ \leq \delta_h \leq 90^\circ
\end{aligned}
\tag{5.6}
$$

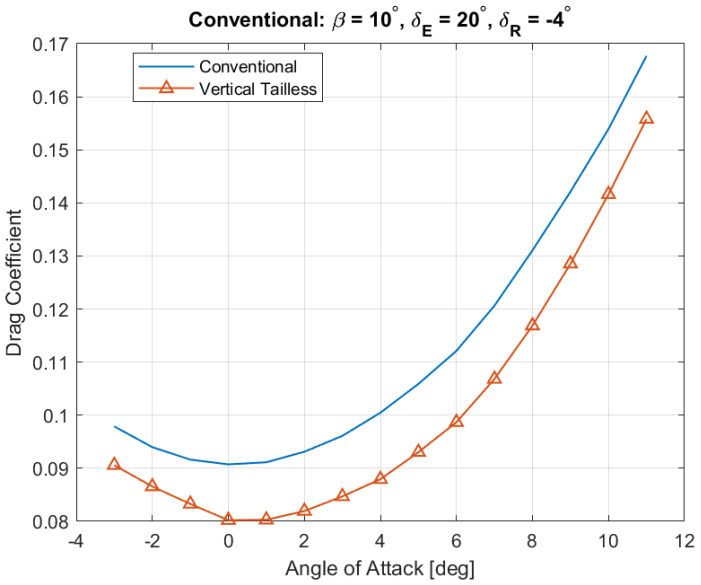

Figure 5.39: Drag Coefficient vs Angle of Attack

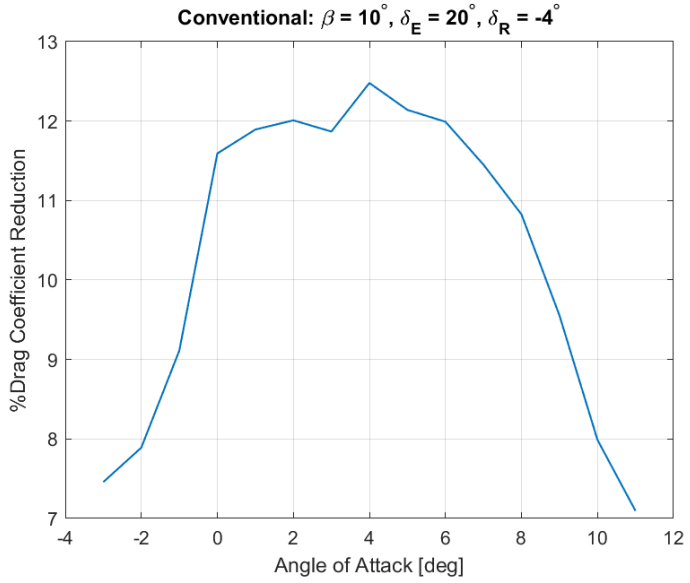

Figure 5.40: Percentage Drag Coefficient Reduction vs Angle of Attack

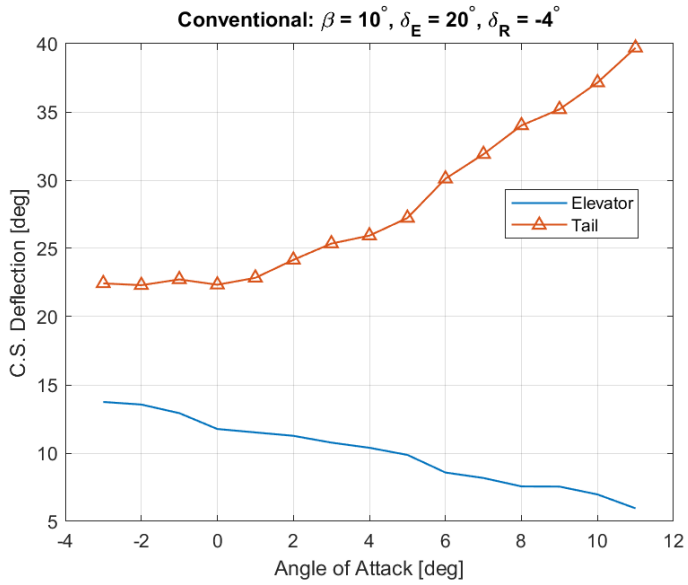

Figure 5.41: Control Surface Deflection Angle vs Angle of Attack

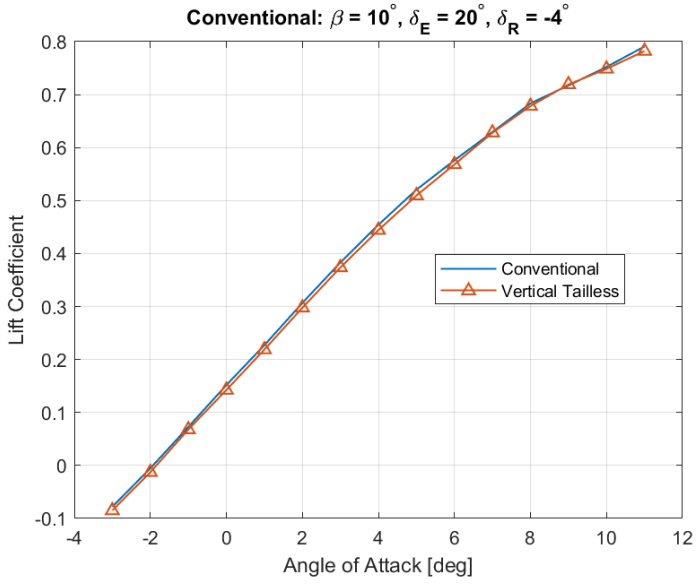

Figure 5.42: Lift Coefficient vs Angle of Attack

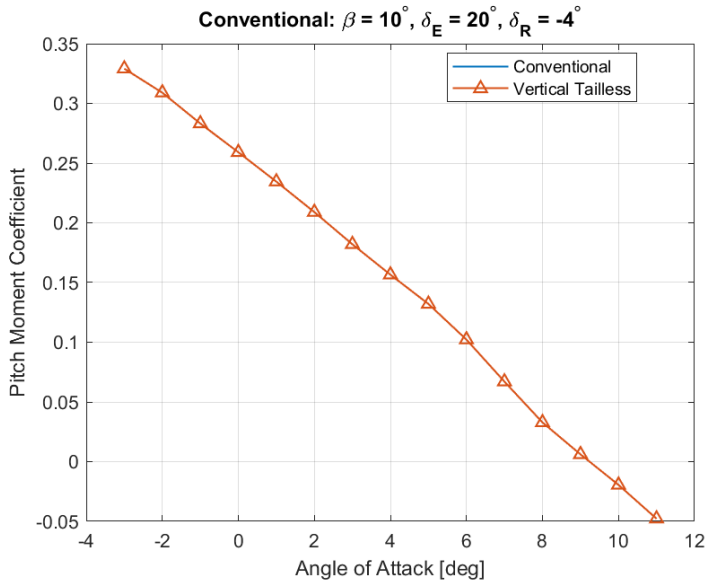

Figure 5.43: Pitch Moment Coefficient vs Angle of Attack

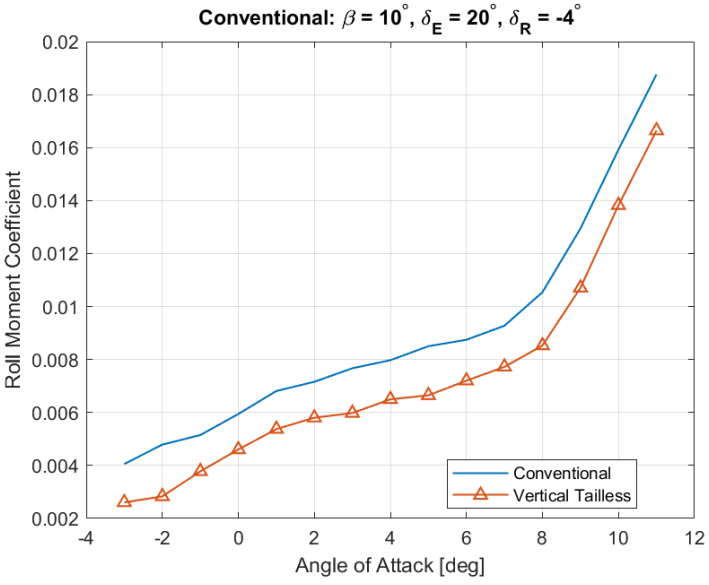

Figure 5.44: Roll Moment Coefficient vs Angle of Attack

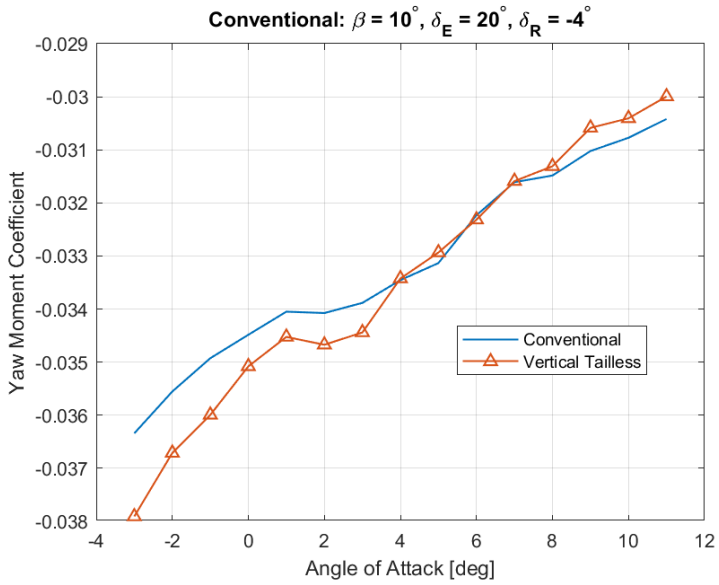

Figure 5.45: Yaw Moment Coefficient vs Angle of Attack

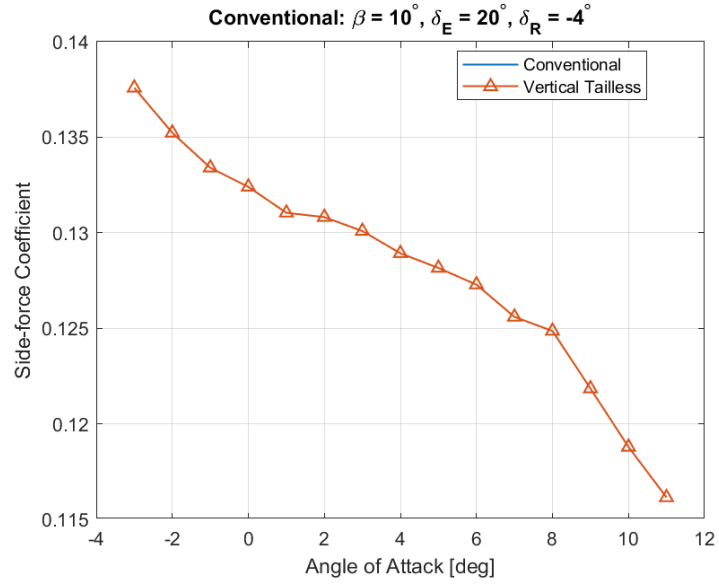

Figure 5.46: Side-force Coefficient vs Angle of Attack

Chapter 6

CONCLUSIONS AND FUTURE WORKS

In this thesis, we have explored the possibility and merit of replacing the vertical tail of a conventional aircraft with a rotary horizontal tail from the aerodynamics, stability and control perspective. On the stability and control side, we utilize an generic method to model the nonlinear rigid body dynamics of a conventional aircraft. Then the nonlinear dynamics of the vertical tailless model is obtained by modifying the aerodynamics model. The nonlinear system is linearized at steady level flight conditions and the linearized system is found to be both controllable and observable. Through eigenvalue analysis, it is observed that the Dutch roll mode becomes unstable and the roll mode is stable but oscillatory. Finally, a linear quadratic regulator is designed to show that the vertical tailless aircraft is stabilizable through active control. On the aerodynamics side, the aerodynamic data collected in Kirsten Wind Tunnel for a RV-4 model are analyzed and results have shown that the drag coefficient of the vertical tailless model is reduced by an average of 3.18% comparing to its conventional version for steady level flight, 3.25% for steady level turn, and 10.4% for selected control surface deflection angles.

Although we have found considerable amount of evidence that the vertical tailless aircraft is more aerodynamically efficient than its conventional version, there are still rooms for improvements. For instance, aerodynamic analysis software such as VLAERO+ and XFLR5 either don't include viscous drag or have a poor estimation of it. If someone wants to compare the software generated total drag coefficient to that of the wind tunnel, other software should be used for better viscous drag estimation. The nonlinear dynamics of the vertical tailless RV-4 model can be modeled by replacing the aerodynamics model we discussed in Chapter 4 with the wind tunnel data we presented in Chapter 5. To do that, the aerodynamics data

from the wind tunnel has to be completed by collecting the data with tail rotation angle from 0° to -90° and rudder deflection angle from 0° to 20°. The moment of inertia of the RV-4 model also needs to be measured. The installation of the rotary horizontal tail brings challenges not only in decoupling the longitudinal and lateral dynamics but also in designing suitable control algorithms for the rotary horizontal tail in different flight scenario.

BIBLIOGRAPHY

[1] Bras, M., Vale, J., Lau, F., and Suleman, A., "Flight Dynamics and Control of a Vertical Tailless Aircraft," *Journal of Aeronautics & Aerospace Engineering*, Vol. 2, No. 4, 2013, pp. 1–10.

[2] Kroo, I., "Unconventional configurations for efficient supersonic flight," *VKI Lecture Series on Innovative Configurations and Advanced Concepts for Future Civil Aircraft*, 2005, pp. 2005–06.

[3] Liebeck, R. H., "Design of the blended wing body subsonic transport," *Journal of aircraft*, Vol. 41, No. 1, 2004, pp. 10–25.

[4] Kroo, I., "Tailless aircraft design—recent experiences," *Symposium on Aerodynamics & Aeroacoustics, Advanced Series on Fluid Mechanics*, 1993, pp. 207–229.

[5] Kroo, I., "Design and development of the SWIFT-A foot-launched sailplane," *18th Applied Aerodynamics Conference*, 2000, p. 4336.

[6] Bowlus, J., Multhopp, D., Banda, S., Bowlus, J., Multhopp, D., and Banda, S., "Challenges and opportunities in tailless aircraft stability and control," *Guidance, navigation, and control conference*, 1997, p. 3830.

[7] Stevens, B. L., Lewis, F. L., and Johnson, E. N., *Aircraft control and simulation: dynamics, controls design, and autonomous systems*, John Wiley & Sons, 2015.

[8] Soderman, P. T. and Aiken, T. N., *Full-scale wind-tunnel tests of a small unpowered jet aircraft with a t-tail*, National Aeronautics and Space Administration, 1971.

[9] Cunningham, K., Cox, D., Murri, D., and Riddick, S., "A piloted evaluation of damage accommodating flight control using a remotely piloted vehicle," *AIAA Guidance, Navigation, and Control Conference*, 2011, p. 6451.

[10] Stengel, R. F., *Flight dynamics*, Princeton University Press, 2015.

[11] Sadraey, M., "Design of Control Surfaces," *Aircraft Design: A Systems Engineering Approach*, 2012, pp. 631–753.

[12] Stenfelt, G. and Ringertz, U., "Yaw control of a tailless aircraft configuration," *Journal of aircraft*, Vol. 47, No. 5, 2010, pp. 1807–1811.

[13] Grauer, J. A. and Morelli, E. A., "A generic nonlinear aerodynamic model for aircraft," *AIAA Atmospheric Flight Mechanics Conference*, 2014, p. 0542.

[14] Ugray, Z., Lasdon, L., Plummer, J., Glover, F., Kelly, J., and Martí, R., "Scatter search and local NLP solvers: A multistart framework for global optimization," *INFORMS Journal on Computing*, Vol. 19, No. 3, 2007, pp. 328–340.

[15] Glover, F., "A template for scatter search and path relinking," *Lecture notes in computer science*, Vol. 1363, 1998, pp. 13–54.

[16] Dixon, L. C. W., "The global optimization problem. an introduction," *Toward global optimization*, Vol. 2, 1978, pp. 1–15.

[17] Nathman, J. and McComas, A., "Comparison of stability and control calculations from vortex lattice and panel methods," *46th AIAA Aerospace Sciences Meeting and Exhibit*, 2008, p. 314.

[18] McDonald, R. A., "Advanced modeling in OpenVSP," *16th AIAA Aviation Technology, Integration, and Operations Conference*, 2016, p. 3282.

[19] Phillips, W., Hansen, A., and Nelson, W., "Effects of tail dihedral on static stability," *Journal of aircraft*, Vol. 43, No. 6, 2006, pp. 1829–1837.

[20] Mader, C. A. and Martins, J. R., "Computation of aircraft stability derivatives using an automatic differentiation adjoint approach," *AIAA journal*, Vol. 49, No. 12, 2011, pp. 2737–2750.

[21] Ngo, A., Reigelsperger, W., Banda, S., and Bessolo, J., "Multivariable control law design for a tailless airplane," *Guidance, Navigation, and Control Conference*, 1996, p. 3866.

[22] Babister, A., "Aircraft longitudinal motion at high incidence," *The Aeronautical Journal*, Vol. 83, No. 822, 1979, pp. 230–232.

[23] Welstead, J., "Conceptual design optimization of an augmented stability aircraft incorporating dynamic response performance constraints," 2014.

[24] L'Afflitto, A., *A mathematical perspective on flight dynamics and control*, Springer, 2017.

[25] Dutton Jr, J. P., "Development of a Nonlinear Simulation for the McDonnell Douglas F-15 Eagle with a Longitudinal TECS Control-Law." Tech. rep., AIR FORCE INST OF TECH WRIGHT-PATTERSON AFB OH, 1994.

[26] Weisshaar, T. A., "Morphing aircraft technology-new shapes for aircraft design," Tech. rep., PURDUE UNIV LAFAYETTE IN, 2006.

[27] Dorsett, K. M. and Mehl, D. R., "Innovative control effectors (ICE)," Tech. rep., LOCKHEED MARTIN TACTICAL AIRCRAFT SYSTEMS FORT WORTH TX, 1996.

[28] Roskam, J., *Airplane flight dynamics and automatic flight controls*, DARcorporation, 1998.

[29] Obradovic, B., "Modeling and simulation of the flight dynamics of morphing wing aircraft," 2010.